# Nanoscale imaging of the Woodford Shale, Oklahoma, USA: Organic matter preservation as clay-organic nanocomposites

Thesis submitted in accordance with the requirements of the University of Adelaide for an Honours Degree in Geology

Samuel Alex Fraser

November 2012

THE UNIVERSITY of ADELAIDE

## TITLE

Nanoscale imaging of the Woodford Shale, Oklahoma, USA: Organic matter preservation as clay-organic nanocomposites

## RUNNING TITLE

Nanoscale imaging of the Woodford Shale, Oklahoma, USA

## ABSTRACT

Regional and within well variability in hydrocarbon production from organic carbon-rich shales has demonstrated that these unconventional reservoirs are complex and require an in-depth understanding of geological factors to make successful predictions. Variability is apparent in porosity and permeability, mechanical properties governing fracture susceptibility for enhanced hydrocarbon release, and concentrations of organic carbon (OC). The economically successful, though variable Woodford Shale, Oklahoma, USA, shows a $R^2 = 0.72$ correlation between mineral surface area (MSA) and total organic carbon (TOC) consistent with a mineral surface preservative effect on OC extending across a range of samples from multiple cores and with TOC values of <0.5% to 18%. The TOC and MSA data illustrates the systematic stratigraphic co-variant relationship between TOC and MSA showing steps of up to 15% TOC that are matched by similar shifts in MSA. Transmission electron microscope (TEM) imaging performed on ~80 nanometre thick ultramicrotomed thin sections independently confirms quantitative geochemical clay-OC associations at the nanoscopic scale of interaction. Energy Dispersive Spectrometry (EDS) spot analyses reveal that organic carbon is entirely constrained to nanoscale clay laminae within the sample. Grey zones encapsulated by clay aggregates appear homogeneous at low magnifications and are similar to discrete organic matter particles commonly interpreted in recent studies. However, high resolution inspection resolves these zones in to laminated clay particles occurring at tens of nanometres. TEM micrographs of later stage submicron-scale quartz grain growth may also explain how the opposing mechanisms of hydrocarbon leaching and entrapment can co-exist for over 300 million years and provide an insight into shale brittleness, known to increase fracture susceptibility. Determining key modes of how OC is preserved during deposition and early diagenesis in proven gas-shales, such as the Woodford Shale encompasses a more holistic approach to enhancing the prediction of prospective hydrocarbon resources in frontier basins.

Keywords
Organic matter preservation, clay minerals, quartz grain diagenesis, shale, gas storage, TEM, FIB, EGME, TOC variability.

**TABLE OF CONTENTS**

**LIST OF FIGURES AND TABLES**

## INTRODUCTION

Organic carbon-rich black shales were traditionally regarded in the petroleum industry as homogeneous impermeable units serving as seals or source intervals in conventional petroleum systems (Demaison & Moore 1980, Jahn *et al.* 2008, Hart *et al.* 2011). In the past decade throughout North America, recent developments in hydrocarbon recovery techniques such as horizontal drilling and hydraulic fracturing has enabled economic production of hydrocarbon bearing shales (EIA 2011). Now recognised as self sourcing reservoirs, these organic-rich shales have more than doubled natural gas reserves in North America from 195 trillion cubic feet (Tcf) in 2002 to present (2012) reserves of 482 Tcf (EIA 2012). Shale gas now accounts for approximately 24% of total natural gas production in the United States, and is projected to rise to 45-49% by 2035 (EIA 2011, NETL 2011). Although a general resource potential is recognised, the poor understanding of how to best explore and produce this new energy resource is indicated by the difference in gas production rates regionally and within wells (Jenkins & Boyer 2008, Cooke 2011). 'Trial and error' drilling practices have revealed kilometre-scale zones of high (but variable) hydrocarbon production rates, commonly named 'sweet spots', situated amongst 'dead zones' of poor production (Jenkins & Boyer 2008, Berman 2009, Durham 2010). Highlighting this variability, Berman (2009) estimates that 15% of wells account for 85% of the production in the Mississippian age Barnett Shale, Texas. This demonstrates that shales are not as homogenous as widely believed, but the factors governing shale heterogeneity at various scales are presently not well understood.

Understanding the properties that govern shale heterogeneity is the focused of current research in the geoscience community and petroleum industry. Variability is apparent in

porosity and permeability, mechanical properties governing fracture susceptibility for enhanced hydrocarbon release, as well as concentrations of organic carbon (OC). The controls on the concentration and distribution of OC are of particular interest due to its perceived role as a pivotal factor in hydrocarbon generation. OC concentration has been observed to vary at micrometre, centimetre, parasequence, and regional basin scales (Passey *et al.* 2010, Harris *et al.* 2011, Romero & Philp 2012). Despite the importance of correctly predicting OC-rich source rocks in frontier hydrocarbon exploration, the mechanisms governing organic matter (OM) preservation in sediments are surprisingly poorly understood (Hedges & Keil 1995). Marine sediments are the largest sink for reduced carbon (C) (Berner 1989, Hedges & Keil 1995), but various studies suggest that only ~0.5% of primary OM production escapes remineralisation to be buried and preserved (Arthur & Sageman 1994, Hedges & Keil 1995, Burdige 2007). Variable OC enrichment in marine and lacustrine sediments has been attributed to processes and controls such as dilution by clastic influx (Arthur & Sageman 1994, Tyson 2001, Sageman *et al.* 2003), bio-productivity-driven organic matter flux and supply of terrestrial plant detritus (Lallier-Vergès *et al.* 1993, Smith & Bustin 1998), and favourable oceanographic preservation conditions such as low or depleted dissolved oxygen concentration (sub-oxic, anoxic or euxinic) (Demaison & Moore 1980, Arthur & Sageman 1994, Canfield 1994, Coppola *et al.* 2007, Baumgart *et al.* 2010).

An alternative mechanism is clay mineral driven OM preservation attributed to two separate mechanisms. Studies have shown preservation modes through the physical sheltering of OM by clay mineral aggregates (Ransom *et al.* 1997, Ransom *et al.* 1998, Salmon *et al.* 2000). A quantitative association between mineral surface area and total

organic carbon (TOC) has been observed in both modern and ancient continental margin sediments (Mayer 1993, Keil *et al.* 1994, Mayer 1994, Keil & Cowie 1999, Kennedy *et al.* 2002, Kennedy *et al.* 2006, Curry *et al.* 2007, Kennedy & Wagner 2011). For example, Keil *et al.*(1994) showed organic matter sorption onto clay minerals slowed remineralisation rates by up to five orders of magnitude in modern marine sediments. Similarly, Kennedy *et al*. (2002) correlated 85% of the variation in TOC with mineral surface area (MSA) observed in two organic-rich shale deposits (the Cretaceous upper Niobrara Formation and lower Pierre Shale in Wyoming and South Dakota, USA). These processes have been ascribed to clay minerals having a preservative effect on OC due to polar adsorption of OM onto negative charged interlayer surfaces of clay minerals (Figure 1).

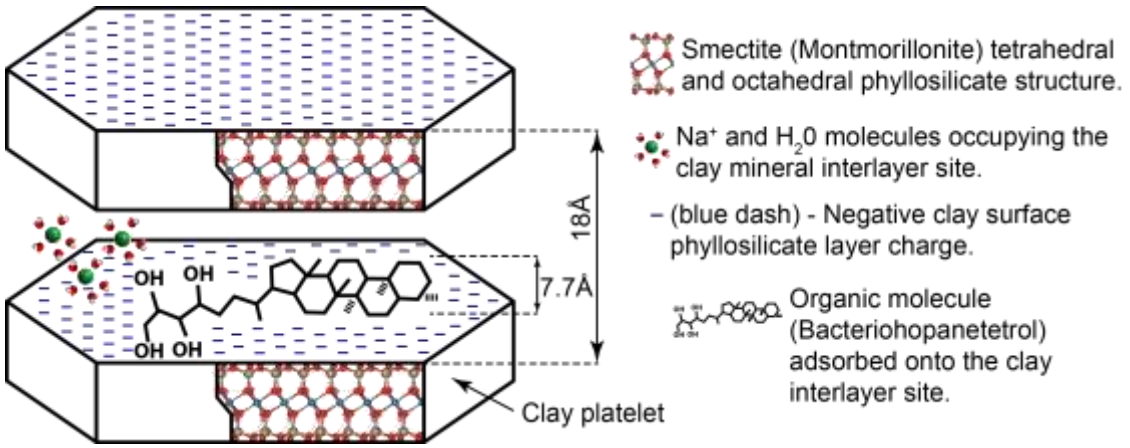


**Figure 1 Three-dimensional schematic showing an example of an organic molecule, in this case - bacteriohopanetetrol, adsorbed onto the interlayer surface site of a clay platelet. Blue dashes (-) illustrate the negative charge at the clay mineral surface resulting from the electron interactions of the aluminium-silicon-oxygen tetrahedral atomic structure. Included are illustrations of the characteristic sodium ions ($Na^+$) and water ($H_20$) molecules occupying the expandable clay interlayer site – in this case, a montmorillonite clay platelet 18 angstroms (Å, 1.8 nanometres) thick. (Note; X and Y scale of platelet is reduced for the purpose of illustration clarity).**

Kennedy *et al.* (2002) and Kennedy & Wagner (2011) have revealed compelling evidence for OM preservation by clay minerals in ancient sediments, however, these studies have relied on bulk sample characterisations. Direct study of OM-clay

associations remains challenging due to the nanometre (nm) scale at which the process occurs. Although useful for observing shale composition and sedimentological structures, standard thin section (~30,000 nm thick) optical petrography, commonly used for coarser grained rocks such as sandstones has proved prohibitive for observing the ~10 angstroms (Å) (1 nm) to ~18Å (1.8 nm) thick clay particles (Moore & Reynolds 1989). Furthermore, the wavelength of visible light (~400 - 740 nm) (Blackman *et al.* 2008) cannot resolve these OM-clay spatial associations. Given the difficulty of nanoscale sample preparation of shales due to their brittle nature, and the nanoscale resolution required to directly image OM-clay interactions, it is not surprising that few images are available.

This study takes a multi-scale approach ranging from outcrop and core to nanometre scale investigations, and includes samples collected across a burial-temperature gradient to test the hypothesis that clay minerals played a key role in the preservation of OC during deposition and through burial in the Woodford Shale, Oklahoma, USA. The Late Devonian-Early Mississippian age Woodford Shale is a classic example of an organic-rich, marine shale featuring geological, and gas production variability (Harris *et al.* 2011, Romero & Philp 2012). Evidence for the Woodford Shale acting contemporaneously as both hydrocarbon reservoir and leeching source rock since ~335 Ma (Higley 2011), adds another dimension to its dynamic nature. In addition to a bulk scale assessment of MSA and TOC associations, this study investigates the possible mechanisms of hydrocarbon storage. By investigating the dynamic properties of a gas bearing, OC-rich shale such as the Woodford Shale, key characteristics governing

carbon preservation, and successful gas production may be determined to enhance the prediction of prospective hydrocarbon resources in frontier basins.

## GEOLOGICAL BACKGROUND

The Woodford Shale is an organic rich marine mudstone of Late Devonian (385 Ma) to earliest Mississippian (Kinderhookian) (359-353 Ma) age deposited in a restricted epeiric sea during a eustatic sea level rise along the west to southwest edge of Laurentia (southern mid-continental North America) (Figure 2) (Lewan 1983, Comer 1991, Lo & Cardott 1995, Blakey 2008).

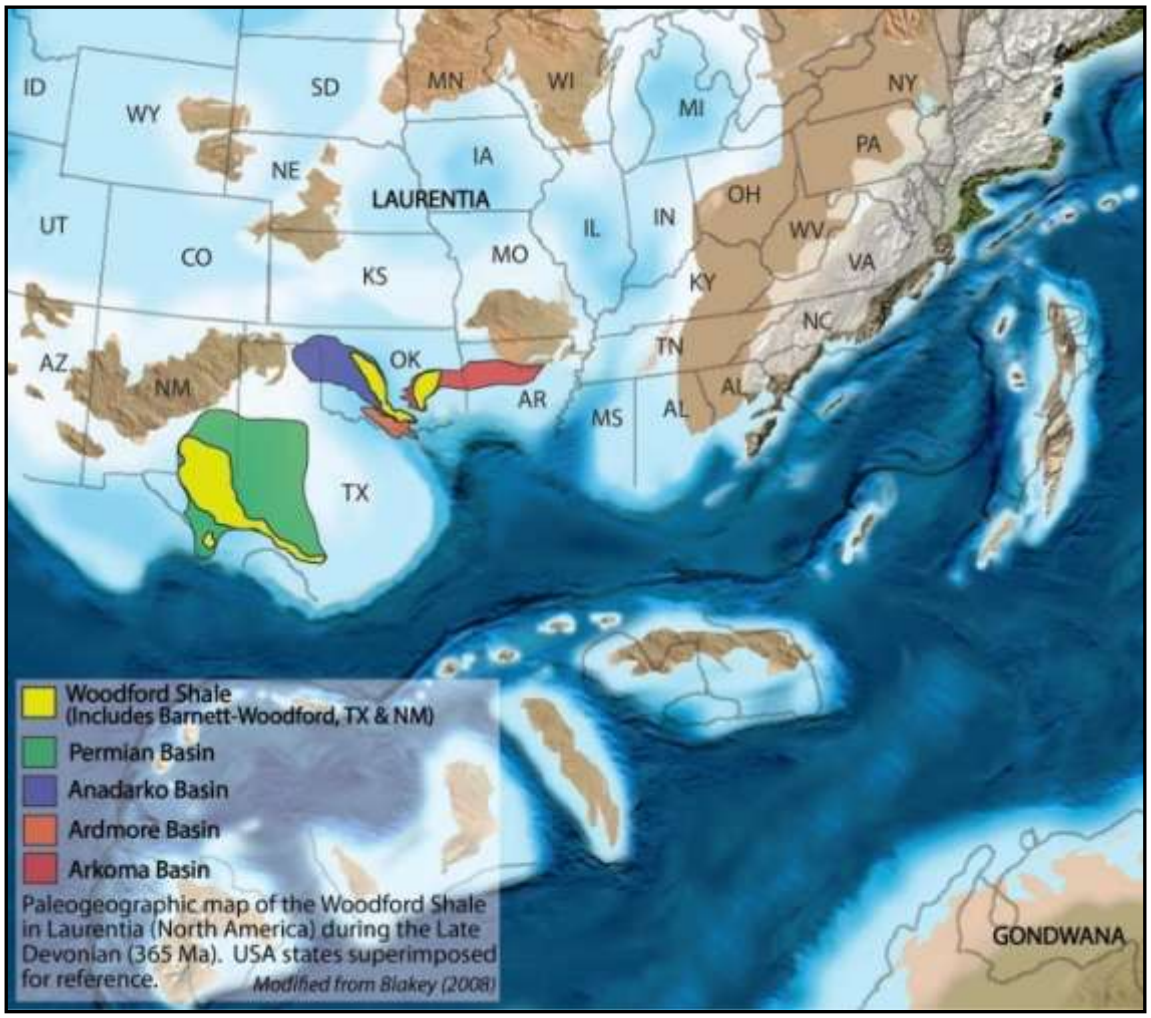


**Figure 2 USA states superimposed on a palaeographic map showing the region of Woodford Shale deposition (south-south-eastern margin of Laurentia) during the Late Devonian (365 Ma). Colour coded regions show the Permian (green), Anadarko (purple), Ardmore (orange) and Arkoma (red) basins wherein the Woodford Shale (yellow) is presently preserved. Modified from Blakey (2008)**

Characterised by the presence of quartz silt, clays, chert, feldspar and dolomite grains, pyritic concretions, framboidal pyrite, siliceous lenses, phosphatic nodules, and calcite concretions (Comer 1991, Harris *et al.* 2011, Romero & Philp 2012), the Woodford Shale is commonly separated into three stratigraphic subdivisions; lower, middle and upper members, based on geochemical and geologic data (Table 1) (Comer 1991, Abousleiman *et al.* 2007, Broadhead 2010, Harris *et al.* 2011, Slatt *et al.* 2011). TOC concentrations in the Woodford Shale typically vary between <1% in siliceous and bioturbated zones constrained to the upper Woodford Shale and up to 20% in the middle and lower Woodford Shale with an overall average of approximately 5% dependant on regional locality (Comer 1991, Broadhead 2010, Harris *et al.* 2011, Romero & Philp 2012).

Table 1 List of the typical geochemical and lithological characteristics defining the upper, middle, and lower Woodford Shale Members (Comer 1991, Abousleiman *et al.* 2007, Broadhead 2010, Harris *et al.* 2011, Slatt *et al*. 2011).

| Upper Woodford | Middle Woodford | Lower Woodford |
|---|---|---|
| • Relatively higher quartz content<br>• Low TOC<br>• High frequency centimetre-scale inter-bedded siliceous layers.<br>• Bioturbation (regionally dependant)<br>• Relatively higher biogenic silica content | • High clay content<br>• High TOC<br>• Very fine alternating planar laminae, and macro-microscopically massive intervals. | • Relatively moderate quartz content<br>• Moderate to high clay content<br>• Moderate TOC<br>• Systematic variations in geochemical and lithological patterns indicative of sea level fluctuations<br>• Relatively low biogenic silica content |

Deposition ceased at different localities during the late Famennian to late Kinderhookian. This is marked disconformably in the west during a period of epeirogenic uplift, and conformably in the central regions during sea level fluctuations and variable sedimentation rates (Comer 1991, Harris *et al.* 2011, Romero & Philp

2012). The basal Woodford Shale in central and southern Oklahoma corresponds to the Misener-Sylamore Sandstones, and unconformably overlies Silurian Hunton Group carbonates and Ordovician Simpson Sandstones (Figure 3). The upper Woodford Shale is bound conformably by the Sycamore and Mississippian Limestones, and Caney Shale varying between basins (Comer 1991, Kuykendall 2001, Comer 2008, Romero & Philp 2012).

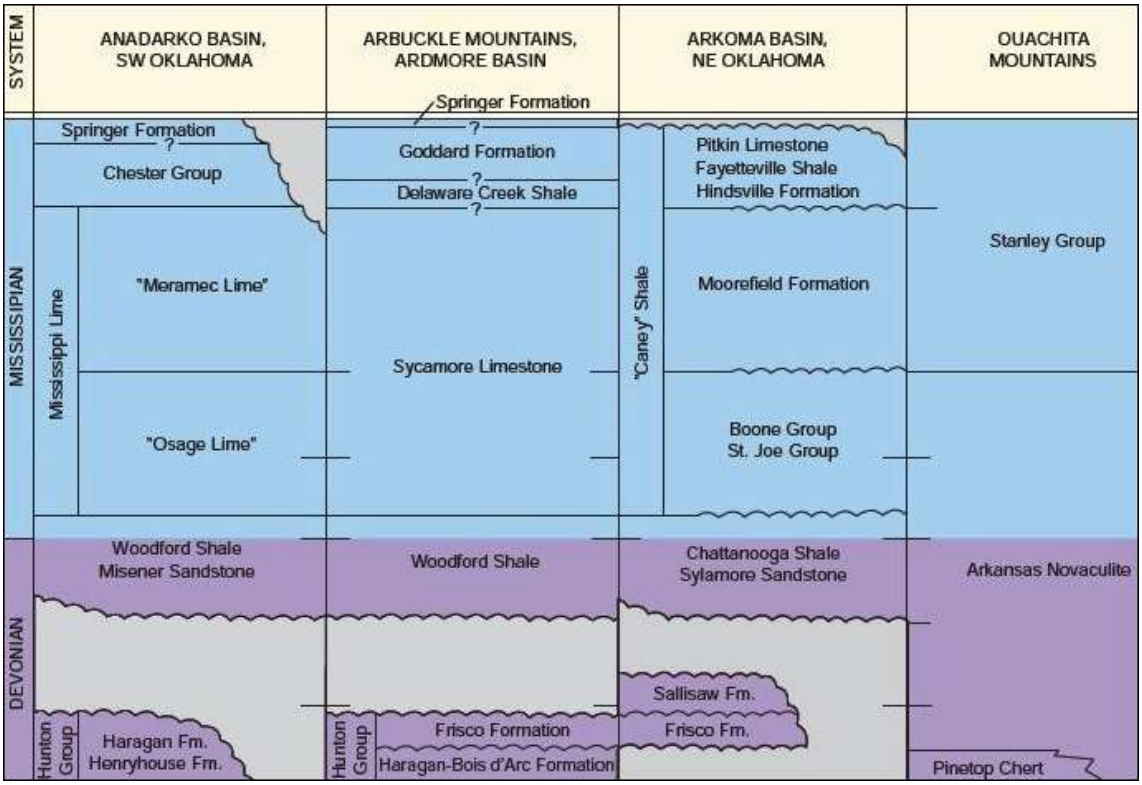


**Figure 3 Stratigraphic chart of the Woodford Shale and binding strata in various basins throughout Oklahoma, USA. Adapted from Cardott & Chaplin (1993) and Comer (1991)**

The Woodford Shale is preserved within a series of basins in modern day Texas, Oklahoma and southeastern New Mexico, USA (Figure 2) (Comer 1991, Harris *et al.* 2011, Romero & Philp 2012) reaching thicknesses of 200 metres in the basin centres, and limited to 30 m at basin margins (Comer 1991, Harris *et al.* 2011). Outcropping in various locations in southeastern Oklahoma the unit also reaches burial depths of 6,000 m in various basin localities (Lo & Cardott 1995, Harris *et al.* 2011, Slatt *et al.* 2011,

Romero & Philp 2012). As a result of frequently sufficient burial in multiple basins (3000 - 5000 m), the Woodford Shale is a significant hydrocarbon source rock throughout the southern midcontinent (Comer 1991, Kulkarni 2011). Previously only regarded as a source rock throughout Texas and Oklahoma, the Woodford Shale is now, however, additionally considered a significant self-sourcing hydrocarbon reservoir (Lo & Cardott 1995, Harris *et al.* 2011, Kulkarni 2011, Romero & Philp 2012).

## METHODS

### Sample Collection

Samples were collected from two cores (East Fitts and Chitwood-Harris) stored at the Oklahoma Geological Survey, USA. Previously attained outcrop samples were collected by M. Kennedy in 2000 from a road-cut outcrop along the south bound lane of Interstate 35 (I-35) situated on the south flank of the Arbuckle anticline in the Arbuckle Mountains of Carter County, Oklahoma, USA (Figure 4). The East Fitts (drilled in Pontotoc County) represents a shallow buried (1,033 - 1,043 m) sample set, whilst the Chitwood-Harris (drilled in Grady County) (Figure 4) represents a deeply buried (4,539 - 4,554 meters) sample set. The samples were selected to capture the geochemical and diagenetic variability over a burial gradient, as well as the sedimentological variability of the Woodford Shale.

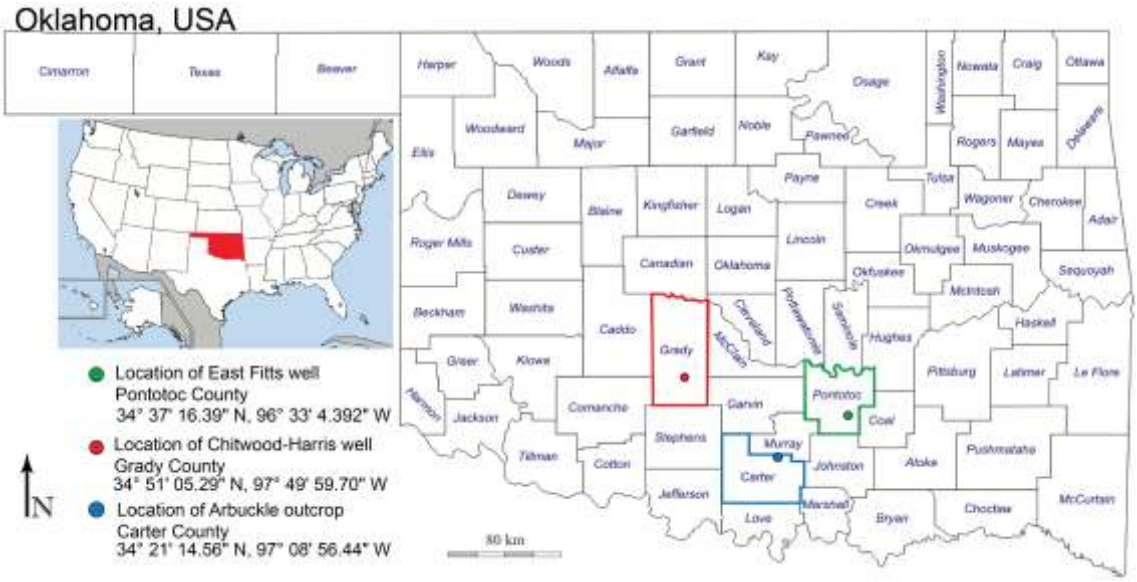


**Figure 4 Map of Oklahoma and Counties, USA showing locations of the East Fitts.**

## Geochemical Analysis

A total of 85 sub-samples (24 from the Arbuckle outcrop, 20 from East Fitts, and 41 from Chitwood-Harris), were milled to a fine powder. MSA was determined using the 'free surface' Ethylene Glycol Monoethyl Ether (EGME) method of Tiller & Smith (1990) (detailed further in Appendix A, Methods), and is reported as silicate MSA on a OC and carbonate free basis to avoid the effects of carbonate dilution which could result in an auto correlation between TOC and MSA. Carbonate does not have a significant surface area (<15 $m^2g^{-1}$) and can result from post burial processes. Total carbon (TC) content for each sample was measured in a LECO TruMac CN analyser and inorganic carbon (IC, as carbonate) content was determined using the pressure-calcimeter method of Sherrod *et al.* (2002). OC content was calculated by difference (TC-IC), and is reported on a carbonate-free basis (i.e. corrected for carbonate dilution). Thermal maturity based on Methyl Phenanthrene Index (MPI) was obtained from thermal extractions using micro-scale sealed vessel gas chromatograph-mass spectrometry

(MSSV-GC-MS) following methods by (Peters *et al.* 2005) (detailed further in Appendix A, Methods).

## Mineralogy

The bulk mineralogy of selected samples was determined by powder X-ray diffraction (XRD; Bruker D8 Advance XRD with Cu source), using Bruker DIFFRAC.EVA software and Crystallography Open Database reference patterns. Micronised sub-samples were prepared for clay fraction and authigenic quartz XRD by settling from an aqueous solution onto a silicon slide. Analysing for ratios between intensity diffraction peaks $I_{100}$ and $I_{101}$ greater than 0.23 (detrital quartz value) (Eslinger *et al.* 1973) indicated authigenic quartz phase in samples. Clay mineral fraction XRD was performed on oriented samples following the methods of Moore & Reynolds (1989) and identified after various treatments (air dried, treated with ethylene glycol, heated to 400˚C and 550˚C for 1 hour) using the USGS Clay Mineral Identification Flow Diagram by Poppe (2001).

## Petrography

To investigate textural and compositional properties, reflected and transmission light optical petrography using a Nikon LV100 POL microscope was performed on twenty representative polished thin sections (~30 microns thick) prepared by Pontifex & Associates Pty Ltd.

Scanning electron microscope (SEM) imaging was carried out on polished blocks and polished thin sections using a FEI Quanta 450 and a Philips XL30.

Transmission electron microscope (TEM; Philips CM 200) analysis of shale ultra-thin sections using Energy Dispersive Spectrometry (EDS) spot analyses at spot sizes 5 (100

nm) and 6 (80 nm) was conducted to investigate the nanoscale association of clay minerals with OM in intact samples. Two different TEM thin section preparation techniques were evaluated for this purpose; diamond knife ultramicrotoming and focussed ion beam (FIB) milling. Ultra-thin sections (~80 nm thick) of osmium tetroxide ($OsO_4$) stained, resin-embedded subsamples (Salmon *et al.*) were cut perpendicular to bedding on a Leica EM UC6 Ultramicrotome and transferred onto carbon-free, silicon dioxide membrane copper grids. TEM thin sections (~100 nm thick sections) of the same samples were also milled perpendicular to bedding using a FEI DualBeam Helios NanoLab 600 focussed ion beam (FIB) and mounted on copper grids. These were prepared with a ~1 micron thick trimethyl-platinum top surface protection coating prior to trench milling at 30 kilo-electron volts (keV), and later polished at 5 KeV following the popular 'lift-out' method published methods (Heaney *et al.* 2001, Wirth 2004, Wirth 2009).

## RESULTS

### Lithological Observations

The thicknesses of the Woodford Shale in the cores and outcrop studied are 11 m (East Fitts), 15 m (Chitwood-Harris) and 55 m (Arbuckle outcrop). It is primarily a thick succession of organic rich shale with intermittent chert intervals (1-10 centimetre thick), but also contains alteration between organic lean siltstone intervals ~0.5-6 metres (m) thick, and intervals hosting pyretic-phosphatic nodules, and cemented siliceous lenses ranging between 0.5 - 6 centimetres (cm) in thickness. Coarser siltstone intervals indicate closer coastal proximity, but lack hummocky beds or sandstones. Absence of

slump structures with only occasional minor indicators of energy preserved as millimetre (mm) scale density current ripples which suggest a quiet depositional environment. Carbonate content is typically low (<1-5%) with the exception of rare fossiliferous centimetre-scale zones). Preserved fossils including tasmanites cysts and radiolaria are concentrated in particular intervals, as well as trace fossils (ichnofabrics) suggesting episodic oxygenated bottom water incursions. The varying intensities of these bioturbated zones were qualitatively determined following the category D Ichnofabric Index (Table 2) defined by Droser & Bottjer (1993).

Table 2 Ichnofabric Index defined by Droser & Bottjer (1993) used for the purpose of qualitatively determining bioturbation intensity within the East Fitts and Chitwood-Harris core samples.

| Ichnofabric Index | Definition |
|---|---|
| Level 1 | No bioturbation recorded - all original sedimentary structures. |
| Level 2 | Discrete, isolated trace fossils, ≤10% of original bedding disturbed. |
| Level 3 | Approximately 10-40% of original bedding disturbed. Burrows are generally isolated, but locally overlap. |
| Level 4 | Last vestiges of bedding discernible; approximately 40-60% disturbed. Burrows overlap and are not always well defined. |
| Level 5 | Bedding is completely disturbed, but burrows are still discrete in places and the fabric is not mixed. |
| Level 6 | Nearly totally homogenised sediment. |

Samples from the Arbuckle outcrop are comprised of interbedded siliceous siltstones and shales with intermittent chert beds throughout the lower 30 m of the exposed section. Coarser siliceous beds dissipate into finely laminated, phosphatic nodule bearing shales, frequently interbedded with chert intervals suggesting this section was deposited in relatively deep water. The upper member contact is not exposed at this locality (Cardott & Chaplin 1993).

The base of the East Fitts core (Figure 3) is comprised of finely laminated shales interbedded with fine (~1 mm thick) siliceous-pyritised laminae (Figure 4a), chert beds (1-4 cm thick), and intervals featuring pyretic-phosphatic nodules (4-20 mm diameter) indicative of diagenesis near the sea floor (Romero & Philp 2012). These planar shales are interrupted at 1,039.3 m by pale to dark brown laminated shales and intermittent zones of black laminated, nodular bearing shales. Pale to dark brown intervals include intermittent sections (1-4 cm thick) of level 2-3 bioturbation (Figure 4b, c) and millimetre-scale density current ripples not observed elsewhere in the core. This implies that these sediments were subject to episodic bottom water currents improving oxygenation at the water-sediment interface. These centimetre-scale alternating bioturbated intervals cease at 1,036.9 m from where there is a coarsening trend to frequent (every 30-100 mm) interbedded siliceous-pyretic lensoid (laminae displacive) beds of silt 0.5-3 cm thick. Coarser sediments dissipate at 1,035.5 m fining upwards throughout the remainder of the core, which consists of very finely laminated planar shale hosting intermittent pyretic laminae (~1 mm thick), chert beds, and intervals hosting pyretic-phosphatic nodules (5-20 mm in diameter).

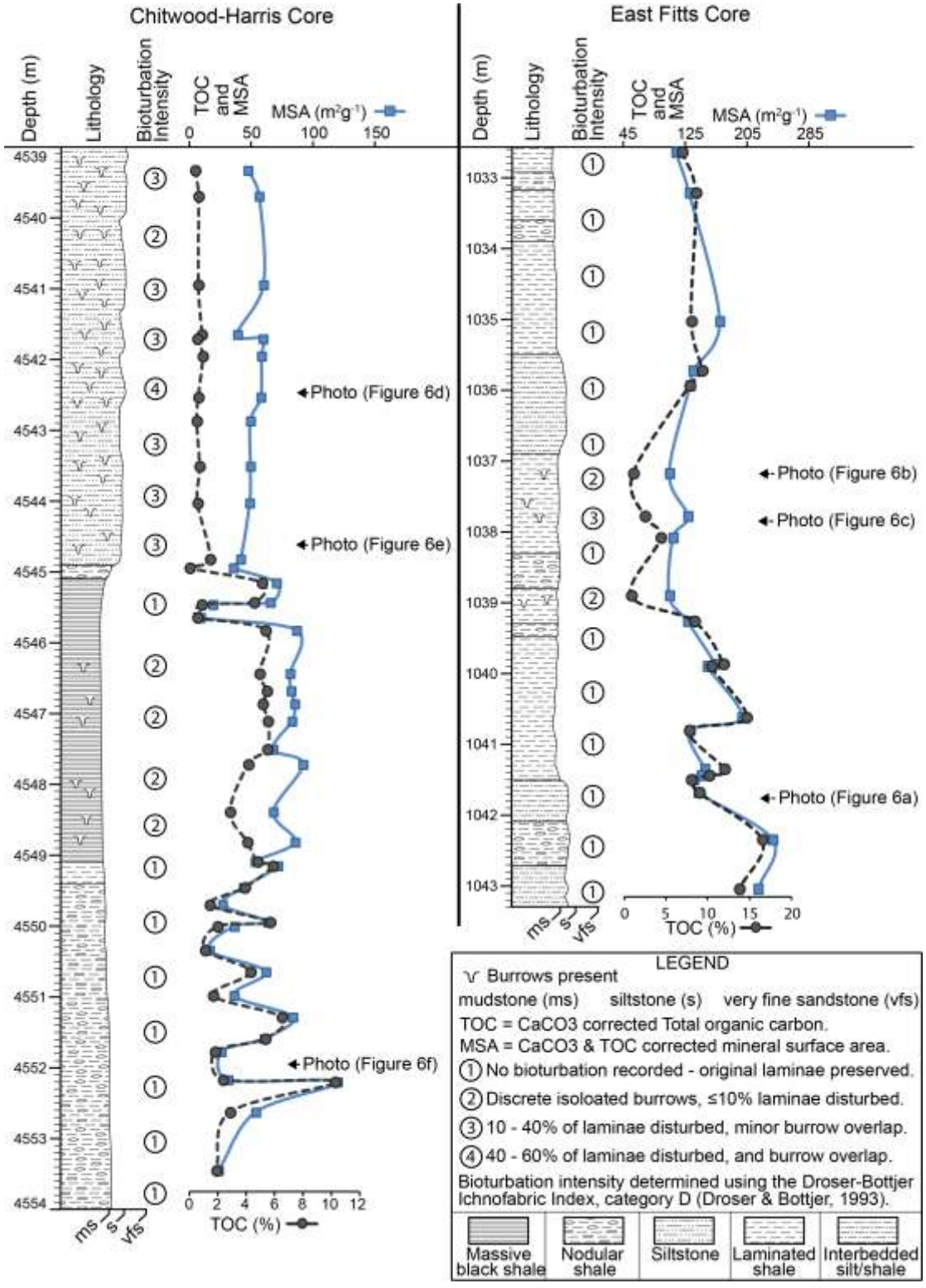


**Figure 5 Core lithology log illustrating the lithological variances in the East Fitts (EF) and Chitwood-Harris (CH) cores. CH displays three distinct lithological zones - phosphatic nodular shale with intermittent siliceous lenses (lower), minor level 2 bioturbated massive shale (middle), and extensively bioturbated (level 2-4) siltstone (upper). EF displays variable lithologies consisting of laminated shales, interbedded siliceous silty shales, and phosphatic nodular shales. Intermittent level 2-3 bioturbation is constrained exclusively to the middle zone. Note that level 1 bioturbation is no bioturbation interpreted. MSA and TOC data matched to depth illustrate the association of bioturbation intensity with poor TOC-MSA correlations.**

The Chitwood-Harris core has three lithologically distinct zones (Figure 3) with varying ichnofabrics (Figure 4d, e). The lower zone (4,554 - 4,549.1 m) is predominantly comprised of finely laminated shales, with occasional intermittent coarser siliceous-pyretic lensoid beds (≤ 5 thick) (Figure 4f) and abundant pyretic-phosphatic nodules (15-80 mm diameter) larger than those in the East Fitts core. Nodules decrease in size and frequency upwards eventually ceasing at the intermediate zone (4,545.1 - 4,549.1) which is comprised of massive black shale with intermittent coarser siliceous beds which decrease in frequency upward. Although difficult to determine due to the complete lack of laminae, this section features minor isolated level 2 bioturbation often as millimetre-scale pyritised shallow burrows. This largely massive unit discontinues at the upper zone (4,539-4,545 m) at which point the lithology is comprised of a dark to light grey siltstone implying a shallowing of the depositional environment. Extensive bioturbation throughout this zone is evident in the form of shallow mm to centimetre-scale burrows indicating a consistent supply of oxygenated bottom water. These burrows show fluctuating disturbance depth in different intervals with the exception of wider centimetre-scale vertical burrows distinctive of a different species. (Figure 4d, e).

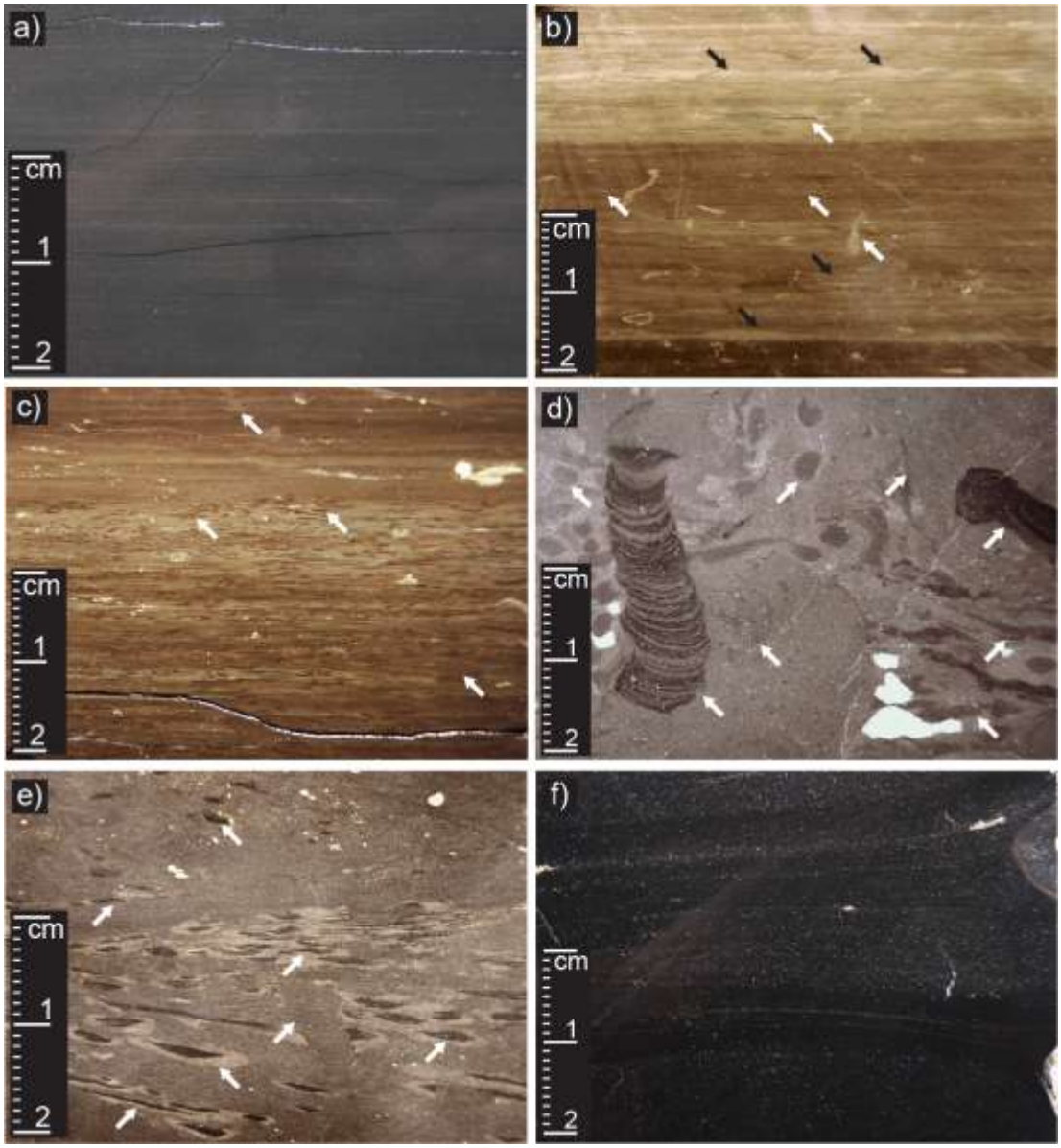


**Figure 6 Digital Photographs of slab-cut core samples showing varying intensities of bioturbation referring to photo locations in Figure 3, and categorised following the Ichnofabric Index by Droser & Bottjer (1993) (Table 2). White arrows mark various examples of trace fossils (burrows), and black arrows indicate density current ripple marks and wavy beds. a) East Fitts (EF) core sample (1,041.7 m) showing a typical sample of very finely laminated shale with very fine pyritised laminae (≤1 mm thick), and does not feature any bioturbation (level 1). b) (EF) Example of density ripple marks (black arrows) and level 2 bioturbation. c) (EF) shows level 2-3 bioturbation featuring overlapping burrows. d) (CH) Example of level 4 bioturbation featuring numerous burrow overlap and extensive laminae disruption. e) (CH) Example of level 3 bioturbation with overlapping burrows and moderate sediment disruption. f) (CH) An example of nodular and siliceous lens growth and consequential laminae displacement.**

## Mineralogical Identification

Bulk powder mineralogy XRD (Figure 7, Table 3) confirmed the presence of clay minerals, quartz, feldspars, dolomite, and pyrite, characteristic of the Woodford Shale. Phyllosilicate minerals matching phengite, clinochlore (chamosite), and muscovite interpreted in bulk XRD were categorised as micas for table simplification (Table 3), however, clay mineral fraction XRD confirmed these as illite and chlorite (Figure 8a), Table 3). Smectite clays were not detected in the samples analysed.

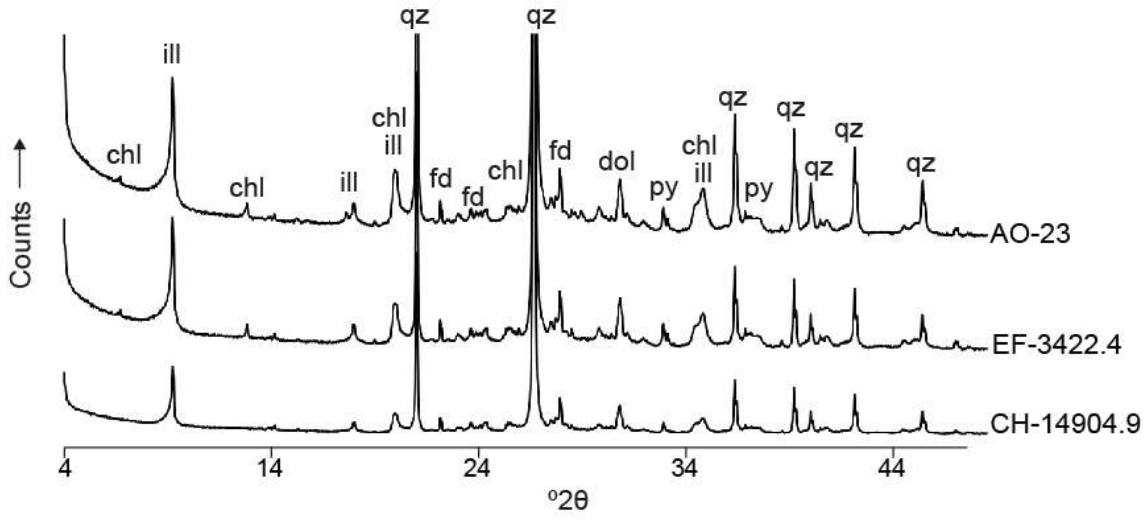


**Figure 7 Bulk powder mineralogy X-ray diffractogram of representative Woodford Shale samples from the East Fitts (EF) and Chitwood-Harris (CH) cores, and the Arbuckle outcrop (AO). Quartz (qz) peaks are dominant throughout all samples, as are phyllosilicate minerals matched phengite, clinochlore (chamosite), and muscovite interpreted in bulk XRD were categorised as either chlorite (chl) and illite (ill) based on comparisons with clay fraction XRD results. All samples showed varying peak intensities of dolomite (dol), pyrite (py), and also alkali and plagioclase feldspars matching multiple types of related mineral species (i.e. albite and anorthoclase). Note, diffractograms have been shifted proportionally above one another and all scaled equally for the purpose of clarity for the average peak intensity.**

Clay mineral fraction XRD (Figure 8a) and various treatments (air dried, treated with ethylene glycol, heated to 400˚C and 550˚C for 1 hour) indicated the presence of chlorite and illite, however chlorite was restricted to East Fitts samples. A lack of swelling and (which would otherwise result in a peak shift) after ethylene glycol (EG) treatment, as well as no peak change after 400˚C treatment, and peak intensity increase

after 500˚C treatment indicate the presence of chlorite. No peak shift, and an increase of intensity post 550˚C treatment confirm the presence of illite.

Table 3 Combined bulk mineralogy, and clay mineral fraction X-ray diffraction (XRD) results of various East Fitts (EF), Chitwood-Harris (CH), and Arbuckle outcrop (AO) samples. 'X' confirms the presence of the corresponding mineral. Quartz (Qz), pyrite (Py), and micas were present throughout all samples. The presence of Dolomite (Dol) and feldspars (Feldsp) varied between samples. Illite is found in all samples, with chlorite restricted to East Fitts samples. N/A indicates that the samples were not analysed for clay mineral fraction.

| Sample | Bulk Mineralogy XRD | | | | | Clay Mineral Fraction XRD | | |
|---|---|---|---|---|---|---|---|---|
| | Qz | Dol | Py | Feldsp | Micas | Illite | Chlorite | Smectite |
| EF-3389.9 | X | X | X | X | X | X | X | |
| EF-3408 | X | X | X | | X | N/A | N/A | N/A |
| EF-3414.4 | X | X | X | X | X | X | X | |
| EF-3422.4 | X | X | X | X | X | X | X | |
| CH-14904.4 | X | X | X | X | X | X | | |
| CH-14916.9 | X | | X | X | X | X | | |
| CH-14934.9 | X | | X | X | X | X | | |
| AO-10a | X | | X | | X | N/A | N/A | N/A |
| AO-17 | X | X | X | | X | N/A | N/A | N/A |
| AO-23 | X | X | X | X | X | N/A | N/A | N/A |

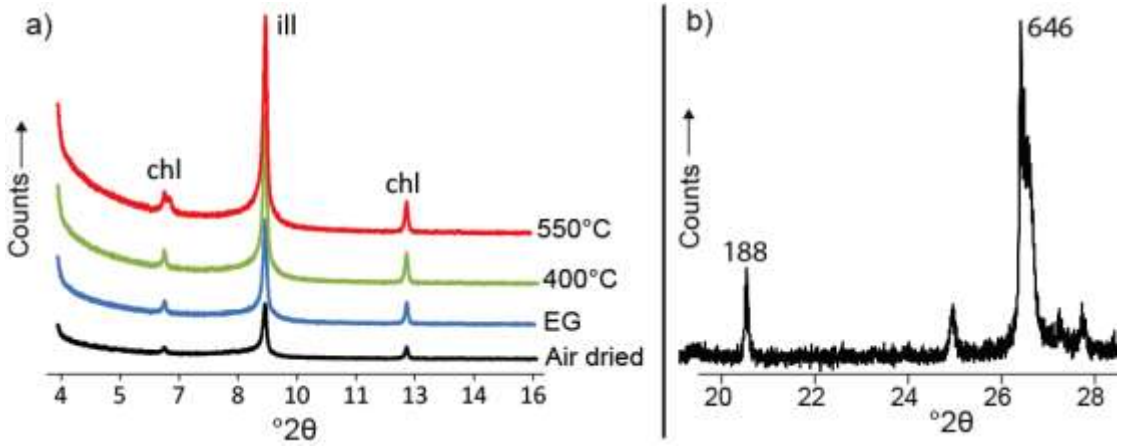


**Figure 8 Clay mineral fraction X-ray diffractograms of a typical East Fitts core sample (EF-3422.4) (a) used to determine the phyllosilicate mineral types following the USGS Clay Mineral Flow Diagram by Poppe (2001). Results indicate the presence of chlorite (chl) which was not observed in Chitwood-Harris samples. Illite (ill) was detected in strong abundance (high counts) in all samples. Note, diffractograms are shifted upwards and separated for figure clarity. b) A zoomed section showing authigenic quartz peak ratios from an X-ray diffractogram of a typical Woodford Shale samples (EF-3422.4). A ratio of intensity diffraction peaks $I_{100}$ and $I_{101}$ and corresponding count values (188 and 646) are used to determine secondary quartz of phase (Table 4).**

Authigenic quartz phase XRD peak ratios (Figure 8b), Table 4) revealed indicative peak ratios varying between 0.27 and 0.36 above the detrital quartz value (0.23) (Eslinger *et al.* 1973), thus confirming the presence of secondary quartz phases in both the Chitwood-Harris and East Fitts samples.

Table 4 Peak Ratio indicates authigenic quartz phase values determined by ratios of quartz intensity diffraction peaks $I_{100}$ and $I_{101}$ (Figure 8b). Peak ratios confirm the presence of authigenic quartz in all Chitwood-Harris (CH) and East Fitts (EF) samples (values all above the detrital quartz ratio of 0.23 as per Eslinger *et al.* (1973).

| **Sample** | **Intensity Peak 100** | **Intensity Peak 101** | **Peak Ratio** (>0.23 = authigenic quartz) |
|---|---|---|---|
| EF-3389.9 | 120 | 433 | 0.28 |
| EF-3414.4 | 144 | 496 | 0.29 |
| EF-3422.4 | 188 | 646 | 0.29 |
| CH-14904.4 | 241 | 901 | 0.27 |
| CH-14916.9 | 282 | 775 | 0.36 |
| CH-14934.9 | 300 | 1064 | 0.28 |

## Geochemical Analysis

Calcium carbonate ($CaCO_3$) and OC corrected MSA and $CaCO_3$ corrected TOC data (tabulated data detailed in Appendix B, Results) show a linear relation (Figure 9) between TOC and MSA in laminated, undisturbed intervals. The undisturbed core samples show strong positive TOC-MSA correlations of $R^2 = 0.95$ (Chitwood-Harris) and $R^2 = 0.82$ (East Fitts), whilst The Arbuckle outcrop samples show a moderate ($R^2 = 0.58$) TOC-MSA correlation due to outlier data attributed to possible causes detailed in the discussion. A poor ($R^2 = 0.29$) relation was evident in bioturbated intervals which are relatively depleted in TOC and feature homogenised MSA values (Figure 5).

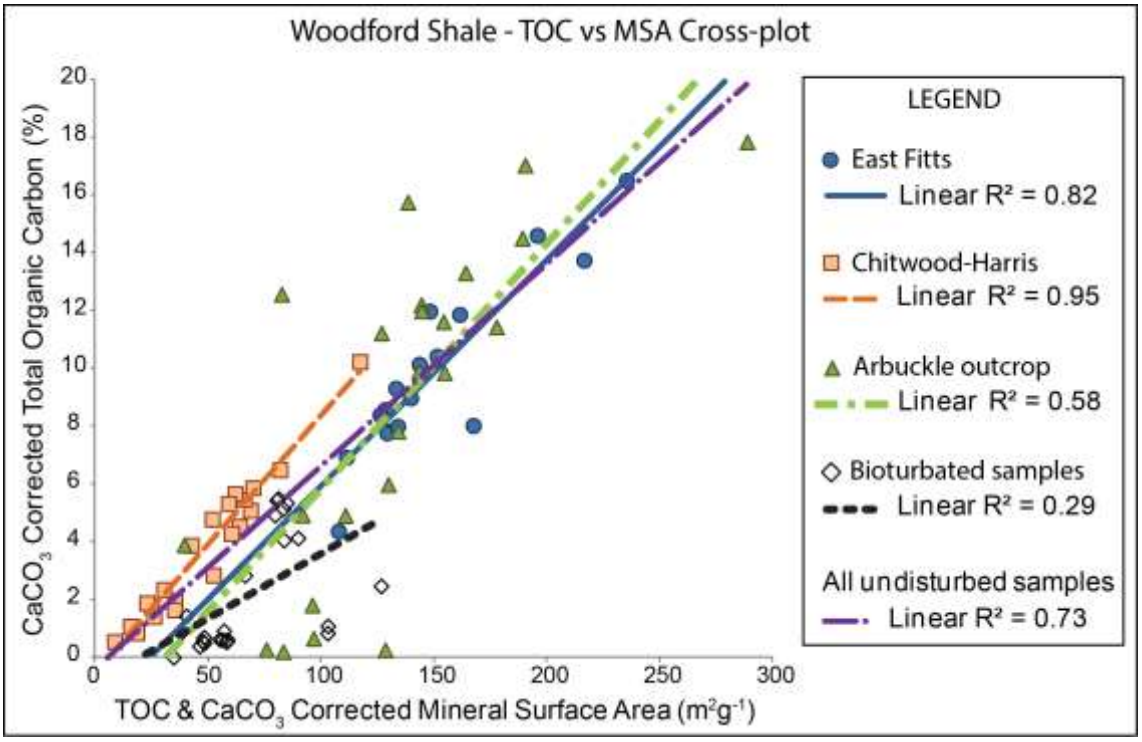


**Figure 9 Total organic carbon (TOC) and $CaCO_3$ corrected mineral surface area (MSA) plotted against calcium carbonate ($CaCO_3$) corrected TOC% for the Chitwood-Harris and East Fitts core samples, and the Arbuckle outcrop samples. Linear regression shows strong positive correlations with $R^2$ = 0.82 (East Fitts) and $R^2$ = 0.95 (Chitwood-Harris). The moderate $R^2$ = 0.58 correlation (Arbuckle outcrop) is possibly due to outcrop weathering effects resulting in OC loss (detailed in discussion), and samples plotting as high TOC to MSA have abnormally high fossil concentrations possibly containing remnant OM not associated with clays. Bioturbated samples are plotted separately ($R^2$ = 29) displaying loss of OC and homogenization of MSA through sediment ingestion and OM digestion by organisms.**

When plotted against sample depth (Figure 10), the TOC and MSA data illustrate the heterogeneity of the MSA and TOC in the cores, and illustrate the systematic stratigraphic co-variant relationship between TOC and MSA. TOC and MSA vary together showing steps of up to 15% TOC that are matched by similar shifts in MSA. Sample to sample shifts closely track between TOC and MSA showing no apparent lead or lag relationship between these two variables. The bioturbated (level 2-4) upper zone (4,539.3 – 4,544.9 m) of the Chitwood-Harrs core presents an exception as TOC is lower (≤1%) and MSA is notably less variable. In addition samples between 4,545.8 and

4,548.8 m depth showing minor level 1 bioturbation had poor to moderate TOC-MSA correlations.

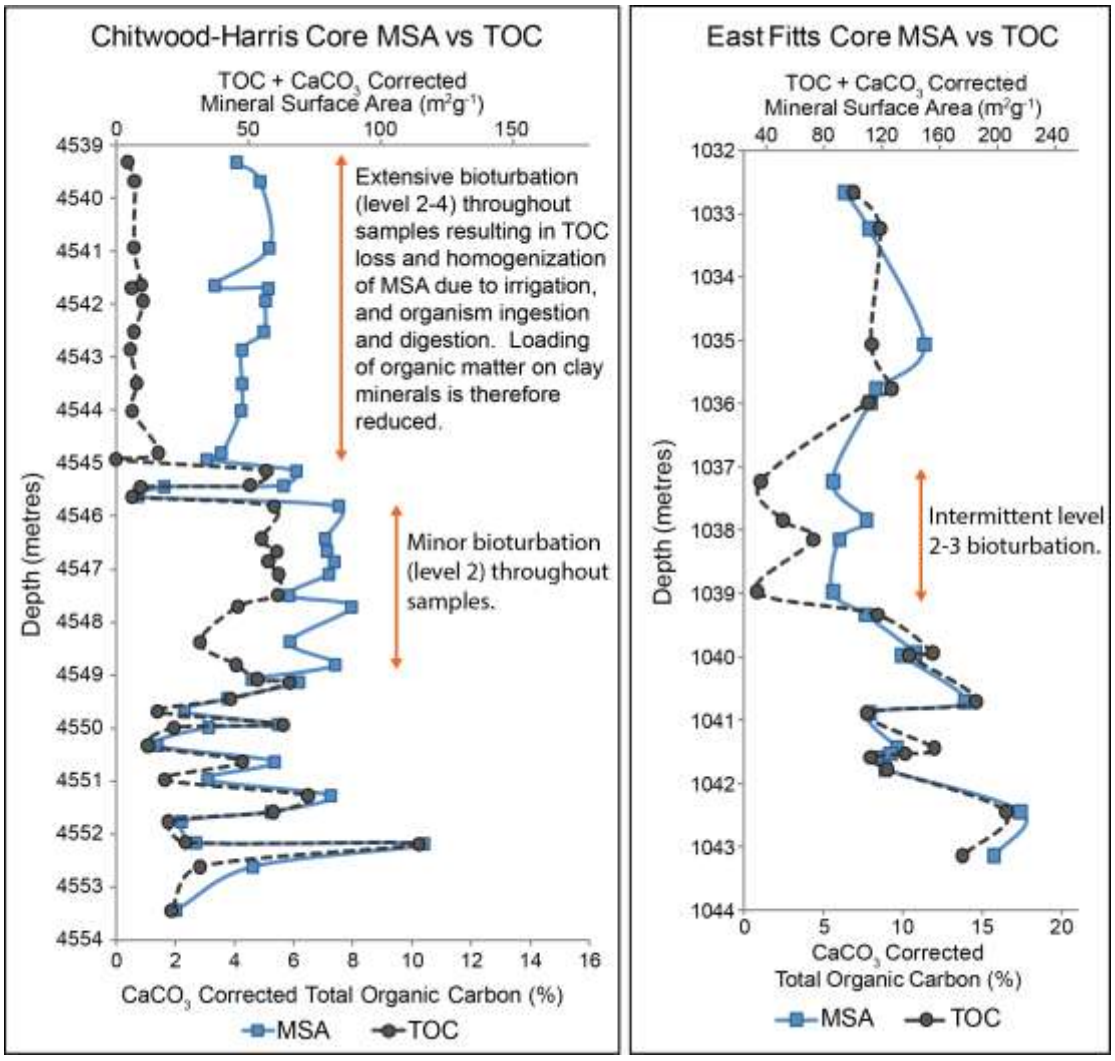


**Figure 10 Organic carbon (OC) and calcium carbonate ($CaCO_3$) corrected MSA plotted against $CaCO_3$ corrected TOC% for the Chitwood-Harris and East Fitts cores according to depth (metres). TOC and MSA with depth illustrates the co-variant relationship of TOC% with MSA on a sample to sample basis that remains in phase. Exceptions to this relationship are two zones (4,539.3 – 4,544.9 m and 4,545.8 - 4,548.8 m) in the Chitwood-Harris core which correspond to varying intensities of bioturbation (level 2-4). This results in both irrigation of sediment, and OM digestion and degradation, leading to significantly reduced OM loading onto minerals and homogenisation of MSA variability prior to burial. The East Fitts core displayed intermittent level 2-3 bioturbation, constrained to the intermediate section (1,037-1,039m) where TOC and MSA do not scale together.**

Thermal maturity for petroleum generation of these cores were calculated based on GC-MS MPI index (see Appendix B, Results) and expressed as calculated vitrinite reflectance ($\%R_o$) (Peters *et al.* 2005). These results show that the East Fitts core with a

0.67% $R_o$ began entering the oil window which ranges between 0.5-0.6%$R_o$ to 1.3-1.35%$R_o$ (Tissot *et al.* 1987, Hunt 1996) for liquid hydrocarbon generation, whereas the Chitwood-Harris core is within the oil window for liquid hydrocarbon generation (%$R_o$ of 1.03).

Samples collected from a road cutting in the Arbuckle Anticline have a mean vitrinite reflectance value of 0.50% determined by reflectance in oil immersion of first-generation vitrinite particles as shown by Cardott & Chaplin (1993) suggesting samples are marginally mature with respect to petroleum generation.

## Multi-scale Petrography of the Woodford Shale

Transmission light and reflected light microscopy (Figure 11) was used to study centimetre to millimetre-scale sedimentary, biogenic and mineralogical features (where grain size was of sufficient scale). At this micron-scale, quartz grains were observable in an amorphous clay matrix (Figure 11a) that was too fine grained to resolve with optical light wave lengths. An anomalous, high carbonate, fossiliferous sample (AO-5), which plotted of the regression line (Figure 9) as high TOC to MSA contained abundant carbonate shell fragments and occasional intact fossils (Figure 11b). Some samples showed sporadic zones (<1 cm thick) hosting preserved organic-rich algal fossils in the form of squashed tasmanite cysts which occurred within more clay dominant intervals as opposed to quartz rich intervals (Figure 11c), but commonly squashed flat from their original spherical shape due to sediment compaction. Tasmanites were either completely pyritised or appear to be organic rich which varied between samples. Pyrite aggregate growths including framboidal pyrite exhibiting laminae displacement (Figure 11d) varied in size (micron to millimetre-scale) and occurrence between samples.

Bioturbated samples (Figure 11e) highlighted millimetre-scale sediment disturbance. Radiolaria rich intervals (Figure 11f) were noted in samples from the lower section of the Chitwood-Harris core (Figure 5). These silica rich fossils, although abundant some samples, did not occur in all samples elsewhere in this lower section. At this scale, no evidence of particulate organic matter could be identified in all thin sections.

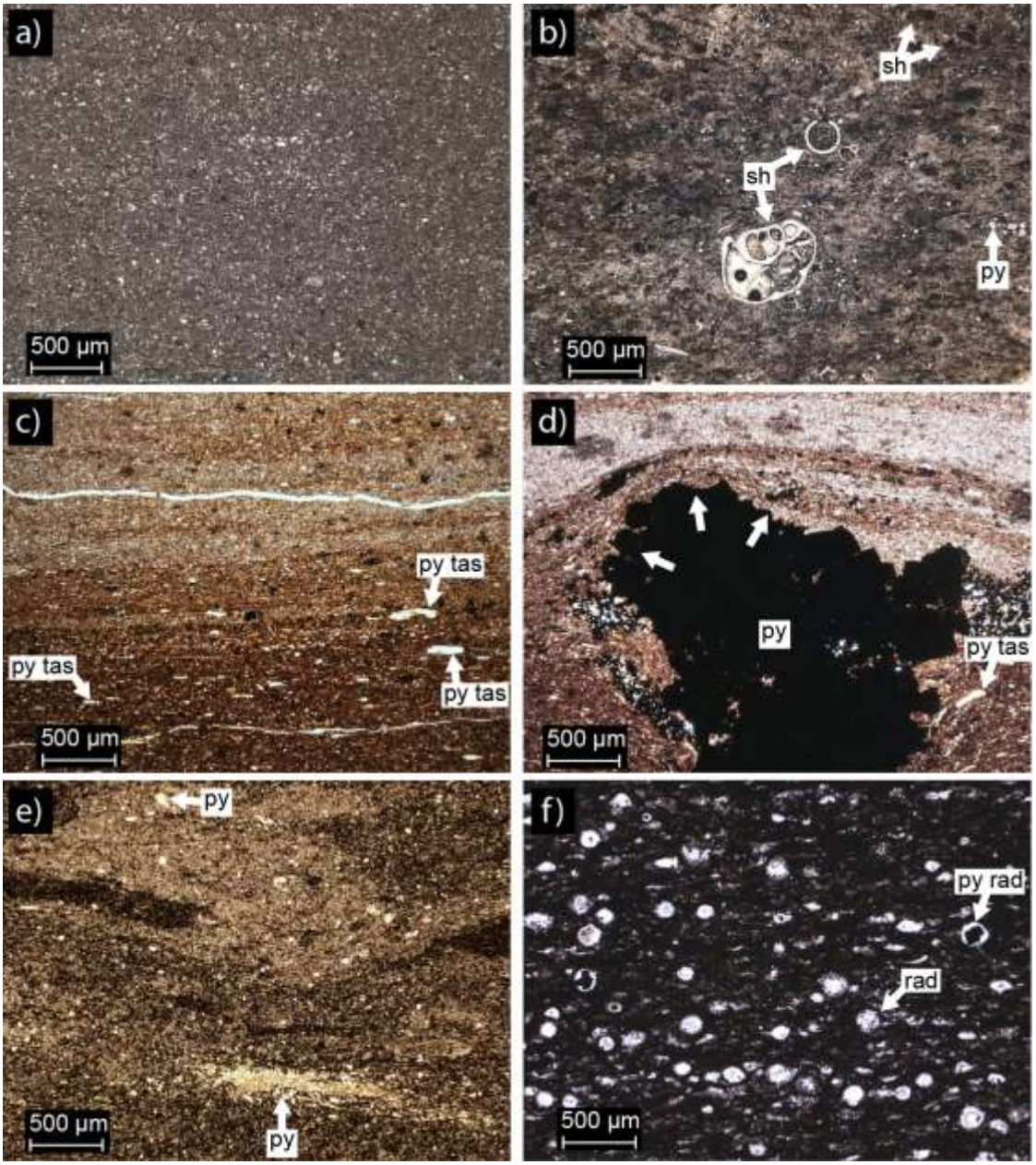


**Figure 11 Photomicrographs of optical thin sections (30 µm thick) examined under reflected and transmission optical light. a) A typical Arbuckle outcrop (AO) sample showing an amorphous clay matrix hosting quartz grains (grey to off-white specs) (10-80 µm in size) and brighter pyrite grains (py) of similar size. b) A rare carbonate fossiliferous AO sample hosting abundant calcareous shell fragments and intact shells (sh) of multiple species. c) East Fitts (EF) sample showing laminae of varying composition (some quartz dominant and some clay dominant). Clay dominant interval hosts pyritised tasmanite (py tas) cyst fossils (three examples indicated) constrained to <1 cm intervals and not always present in other samples. d) EF sample showing laminae displacive pyrite aggregate growth which occur intermittently but are common throughout the Woodford samples. e) Chitwood-Harris (CH) from 4,554 m depth (level 3 bioturbated zone) showing burrowing and disturbance of laminae, and pyrite aggregates (py). f) CH sample from 4,552 m depth showing abundant siliceous radiolaria (rad) fossils (two examples indicated) preserved in an amorphous clay matrix with some radiolaria fossils occasionally hosting pyretic cores (py rad).**

Scanning electron microscope (SEM) imaging was performed on polished blocks and thin sections to confirm organic carbon-rich tasmanites cysts (algal fossils) (Figure 12) using Energy Dispersive Spectrometry (EDS) spot analyses. These tasmanites fossils are not consistent throughout, but rather concentrated in specific <1cm intervals. Such intervals are sporadic and were not present in some samples. Whilst easily distinguished, tasmanites cysts and other visible particulate organic matter are unlikely to provide a significant component of the TOC because of irregular distribution and sporadic occurrence.

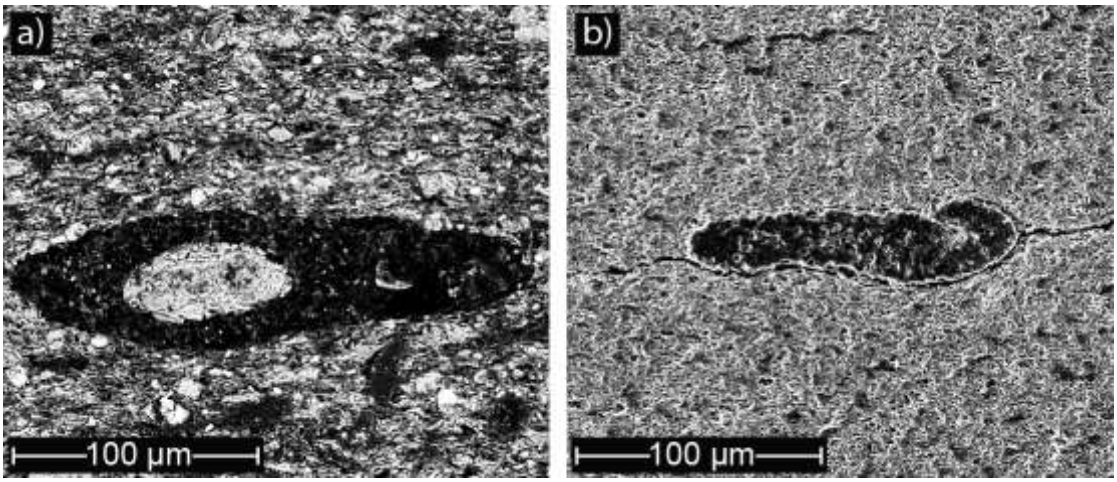


**Figure 12 Scanning Electron Microscope (SEM) images of polished thin sections and polished blocks. a) Back scatter electron (BSE) image shows a squashed organic-rich (darker proportion) tasmanite cyst (~200 µm in length) with a microcrystalline core (light proportion) preserved within a clay-quartz matrix. b) Secondary electron image of a squashed tasmanite cyst (~120 µm in length) preserved within a clay-quartz matrix. Organic-rich fossils are either constrained to mm scale zones, sparsely distributed or not present in some samples.**

## NANOSCALE IMAGING FROM TEM

Transmission Electron Microscope (TEM) micrographs of ultra-thin sections (Figure 13) from the shallowly buried East Fitts core show nanoscale clay laminae separated by diagenetic quartz with inclusions of pyrite, dolomite and quartz grains throughout the clay laminae. Mineralogy was confirmed with Energy Dispersive Spectrometry (EDS) spot analyses identifying elemental chemistry at 80-100 nm resolution. Clay-rich

intervals consist of laminated clay aggregates which are oriented parallel to the shale laminae plane. Examples of EDS spot analyses (Figure 14) performed on clay aggregates (Figure 14a, b, c, d) indicate clays are illitic and contained significant quantities of carbon. OC was not found outside clay-rich zones (Figure 14e, f) and no organic particles were observed in sample EF-3422.4. The grey zones encapsulated by clay aggregates (Figure 15a) appear homogeneous at low magnifications and are similar to organic matter 'blebs' described in Salmon et al (2000). However, closer inspection (up to 120,000 x magnifications) also resolves these zones in to laminated clay particles occurring at tens of nanometre scales (Figure 15b, c). Close inspection of resin indicated a clear boundary at the edge of the sample indicating a lack of penetration into the sample, this lack of permeability was also confirmed from the lack of $OsO_4$ which also did not penetrate into the sample, as it was not detected by EDS spot analysis.

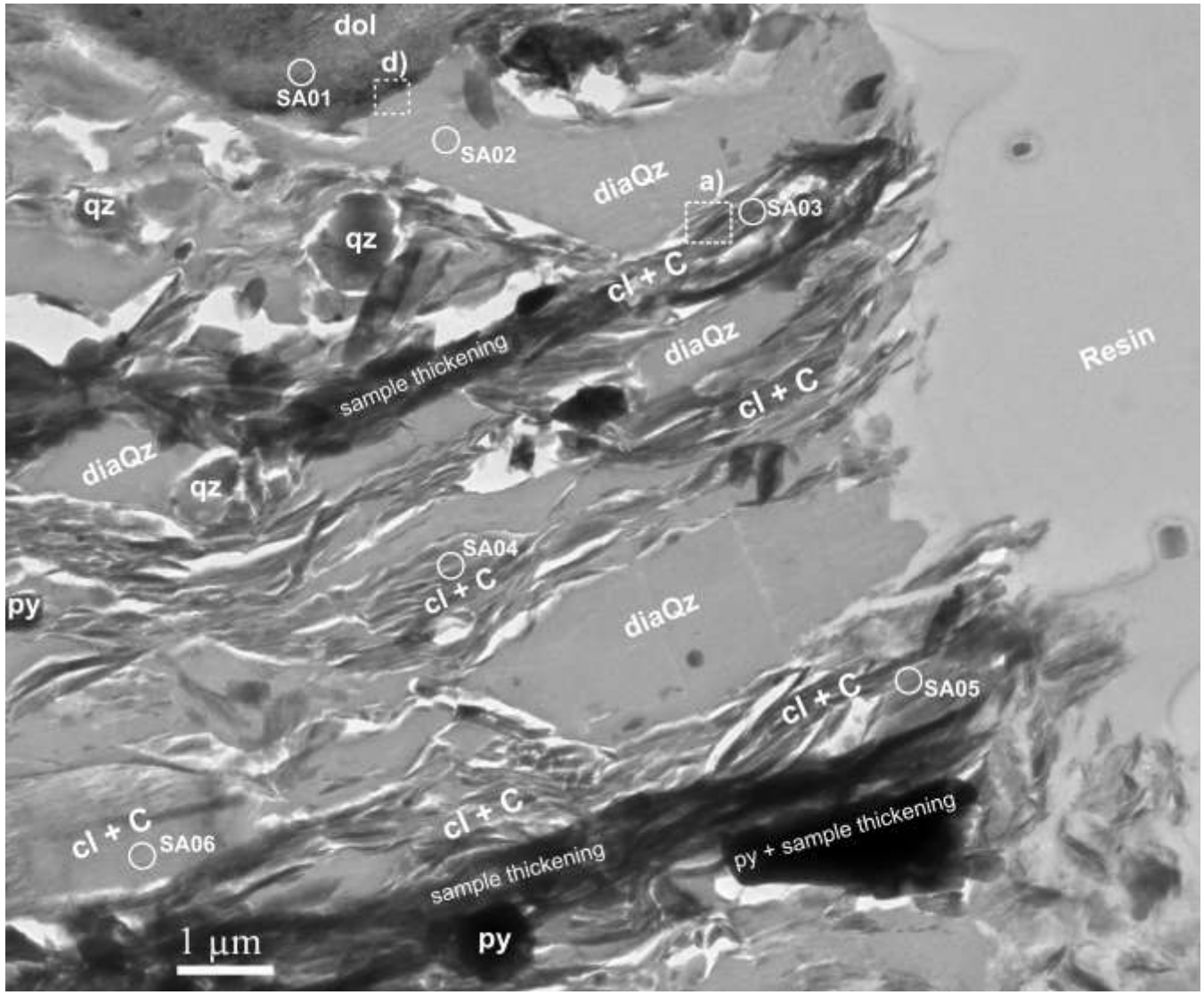


**Figure 13: TEM photomicrograph of an ultra-thin section from the East Fitts core (sample EF-3422.4). Organic carbon (OC) is hosted exclusively within clay layers where it forms a clay-organic nanocomposite (cl+C). Clay layers are planar to shale laminae 300 – 900 nm thick) separated by diagenetic quartz labelled 'diaQz'. Note; dolomite (dol) grain at top left, and quartz grains (qz). 'SA' marks locations of elemental spot analysis by Energy Dispersive Spectroscopy (EDS) shown in Figure 14. Dark zones result from sample thickening or pyrite grains (py) (darkening resulting from a higher density contrast). Resin ceases at the edge of the sample indicating a lack of penetration into the sample. $OsO_4$ also did not penetrate into the sample, as it was not detected by EDS spot analysis. Spot analysis on resin showed minute counts of carbon compared to that carbon detected within clay layers. Dashed squares labelled a) and d) outline areas of zoomed in photomicrographs featured in Figure 15.**

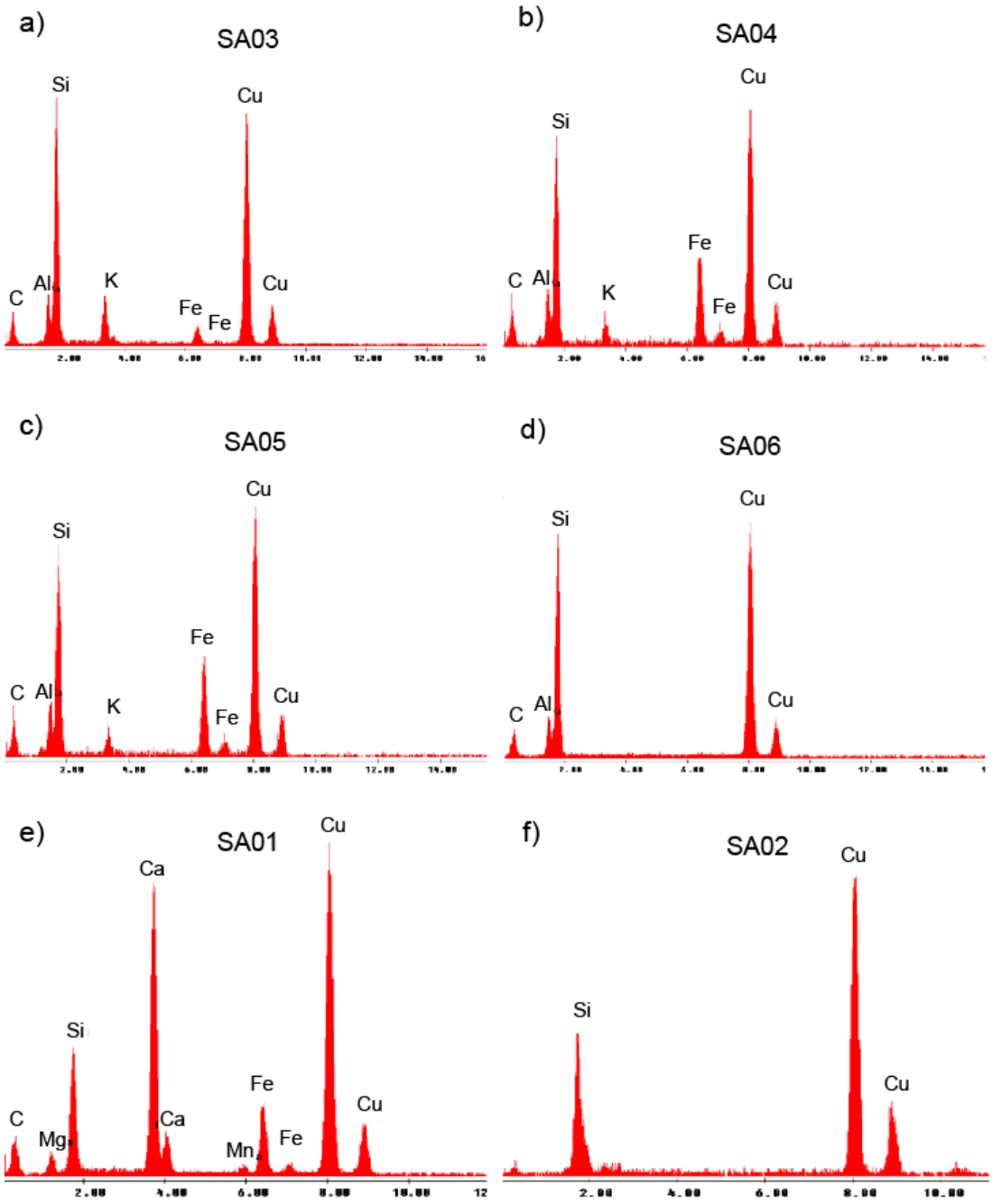


**Figure 14 Examples of energy dispersive spectroscopy (EDS) spot analyses (SA) at spot size 5 (100 nm) and 6 (80 nm) performed throughout the East Fitts 3422.4 sample (see Figure 13 for locations). Peaks in silicon (Si), aluminium (Al), iron (Fe), potassium (K) and carbon (C) (a, b, c,) confirm the presence of clay-organic nanocomposites in Figure 13. d) shows a different alumino silicate mineral hosting C. e) has been interpreted as dolomite (peaks in Mg, Si, Fe, Ca and C as carbonate), consistent with XRD analysis of the sample. f) shows peaks in Si interpreted as diagenetic quartz and lacks C above minute background levels. All copper (Cu) peaks are resultant from the copper sample holder.**

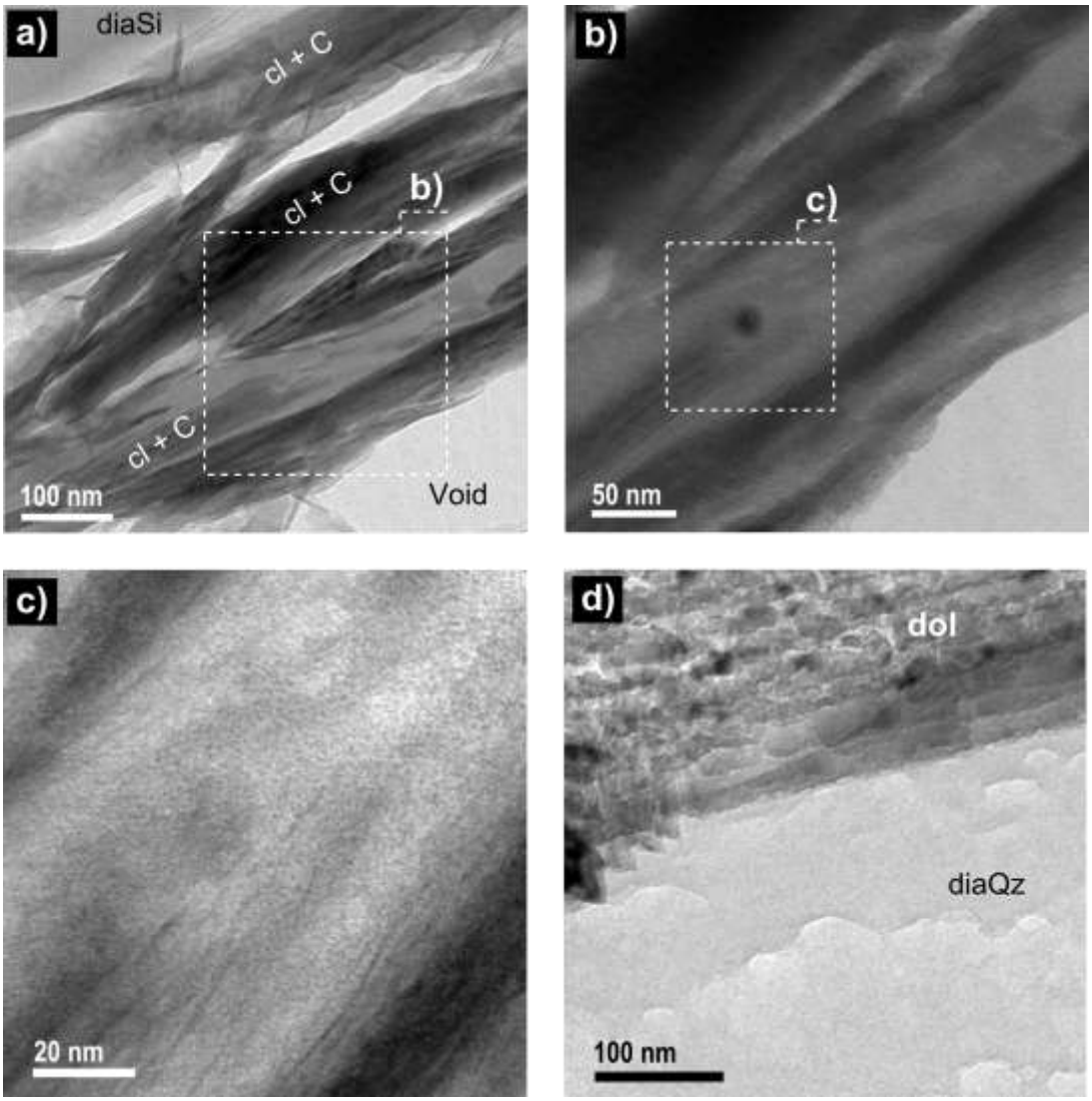


**Figure 15 Zoomed in TEM micrographs of the East Fitts ultra-thin (~80 nm) section shown in Figure 13. Image labels (a) and (d) correspond with dashed squares outlined in Figure 13 and labelled in the top left hand corner. Image a) shows a clay-organic carbon (cl + C) domain hosting what appears as a homogeneous grey area resembling an organic matter blob ~90 nm thick. Dashed squares outline zoomed in images with indicative image labels (i.e. b and c). Higher resolution images (b) and (c) reveal clay lattice fringes (atomic aluminosilicate lattice structures) dispersed within the grey matrix. Darker zones represent thicker (denser) clay layering typically stacked in lens shapes parallel to the depositional laminae. d) shows the interface of a dolomite (Dol) grain and diagenetic quartz (diaSi) nano-layer.**

## MICRON-SCALE QUARTZ GRAIN DIAGENESIS AND HYDROCARBON ENTRAPMENT

TEM analyses on a Chitwood-Harris FIB milled thin foil (Figure 16) revealed submicron-scale diagenetic quartz grain growth in the deeper Chitwood-Harris core which are not present in both the ultra-thin section and thin foil from the East Fitts core.

Polyhedral grain shape indicative of quartz grain growth, and systematic displacement of clay aggregate orientation identifies a diagenetic and fabric displacive origin rather than a detrital origin for this quartz. Based on the TEM micrographs, quartz grain growth is likely to result in reduced connectivity of pores and compartmentalisation of clay-organic rich zones. Zones appear to lack connectivity in quartz dominant area suggesting a closed environment at nanometre and micron scales. Clay rich zones lack, although hosting some polyhedral quartz grains show connectivity between clay-organic zones suggesting higher permeability.

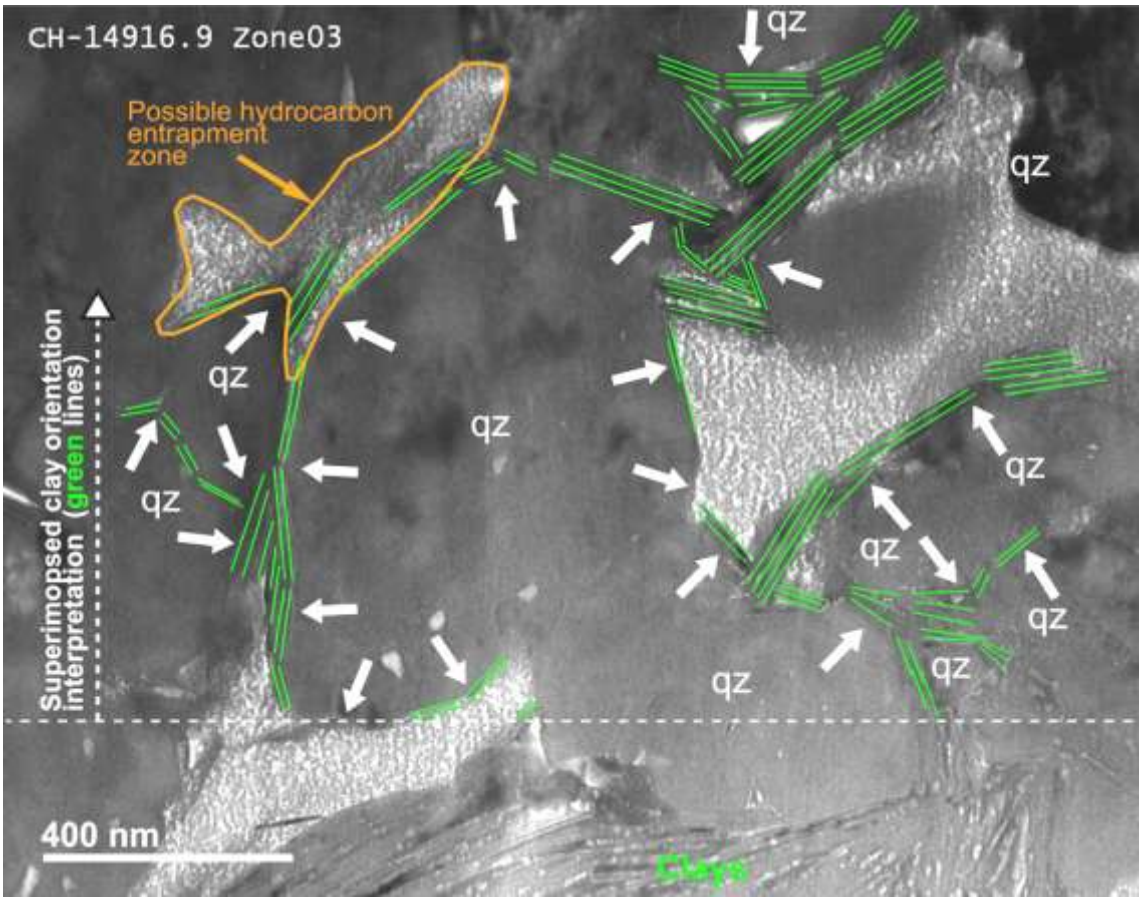


**Figure 16 TEM micrograph of a FIB milled thin foil from the Chitwood-Harris core at 4,546 m depth. Micron-scale quartz grains (qz) exhibiting polyhedral grain shape and systematic displacement of clay particles, indicative of in situ quartz grain growth. White arrows indicate quartz growth direction causing displacement of clay particles (clay lattice fringe orientation) illustrated by green lines. These lattice orientations were determined at higher magnifications throughout the sample. Included in this image is a hypothetical zone of hydrocarbon entrapment (orange polygon) where upon quartz grain growth may enclose nanometre to micron-scale zones in a three-dimensional environment, thus trapping hydrocarbons during thermal maturation.**

# DISCUSSION

## Clay Mineral Controls on Organic Matter Preservation

Bulk rock and nanoscale observations support the hypothesis that the great majority of OC in the Woodford Shale was preserved due to a mineral surface preservation effect. With increasing burial depth and thermal maturity, the data indicate that scaling of MSA and TOC is retained into the oil window. The difference in TOC between laminated, anoxic intervals and bioturbated intervals identifies a second order control of oxygen concentration on TOC either directly through oxidation rates of OM or indirectly by controlling animal metabolization of OM. MSA availability, however, appears to be a necessary condition for initial sequestration of OC. TEM micrographs independently confirm a relation between preserved organic matter and mineral surfaces by showing an intimate relation at the scale of tens of nanometres.

The strong ($R^2$ = 0.82 and $R^2$ = 0.95) linear relationships between EGME-MSA and TOC (Figure 5, 6) are consistent with other studies by Kennedy *et al.* (2002) and Kennedy & Wagner (2011) who showed that variation in TOC within ancient sediments is correlated with MSA. These studies also showed that the relationship between MSA and TOC scaled to high MSA values unique to smectitic minerals (expandable clays) with interlayer surfaces (300 – 500 $m^2g^{-1}$) capable of accepting some organic compounds (Figure 1) because of their weak layer charge. Their conclusions were that the bulk of OM in organic rich shales was preserved in the interlayer sites of expandable clays where sufficient OC was available to saturate mineral surfaces. The data from the East Fitts and Chitwood-Harris cores however show a significant difference from these studies. MSA are typically in the range of 35 – 150 $m^2g^{-1}$, and XRD (Table 3, Figure

8a) and EDS analysis (Figure 14) show that clay mineralogy is restricted to illite and chlorite (non-expandable clays) rather than smectite in both cores (Table 3). This is also observed in TEM micrographs, which indicate that OM is associated with aggregates of illite at the tens of nanometre scale rather than the ~10Å scales at which illite clays occur. Although some OM may have originally adsorbed onto external surfaces of detrital illite, smectite is known to better preserve OM than illite during early diagenesis (Curry *et al.* 2007), so that it is possible that OM which was initially associated with smectite was subsequently expelled during smectite illitization throughout burial. Illitization occurs during burial and heating to ~110° in which layer charge is increased by Aluminium (Al)+3 substitution for Si+4, and potassium (K)+ ions replace interlayer cations during collapse of interlayer spaces (Williams *et al.* 2001). If this is correct, the OM associated with interlayer sites was expelled during illitization of smectite clays, but may have remained in proximal association with illite aggregates. Illitization is inevitable with progressive sediment burial and commonly coincides with the depths and temperatures of hydrocarbon generation in the oil window (Altaner & Ylagan 1997, Abid & Hesse 2007, Lanson *et al.* 2009). Experimental results show that illitization of smectite associated with simple organic compounds results in polymerization (Williams *et al.* 2005) and could be directly responsible for the formation of more complex organic carbon chains like kerogen (Johns 1979, Alexander *et al.* 1982, Alexander *et al.* 1984).

A correlation between MSA and TOC is not necessarily due to a mechanistic relationship in which mineral surfaces directly protect OC. This correlation could record common environmental influences in the depositional setting that effect both OC deposition and variation in clay mineralogy. For example, correlations between

increasing clay content and TOC have been attributed to enhanced continental runoff containing clay minerals and also resulting in a freshwater lens causing basinal anoxia (Kennedy & Wagner 2011). Such a stratified water column restricts circulation and oxygenation of the shallowing pynocline (water density gradient), commonly suggested to result in organic enrichment in sediments (Stanley 1978, Rohling 1991). However, if high MSA supply coincided with anoxia through continental runoff, and anoxia was the primary control on OM preservation, then TOC and MSA data would likely be somewhat out of phase. The sample-to-sample correlation (Figure10), in which TOC tracks MSA from sample to sample even with shifts of up to 15% TOC, without lead or lag between the two variables, is more consistent with a mechanistic relationship between MSA and TOC. Furthermore, the associations with a particular clay mineral phase like smectite would likely be coincidental and rare, and unlikely to be seen in multiple examples with a similar ratio between TOC and MSA as shown by Kennedy *et al.* (2002) and Kennedy and Wagner (2011) in ancient sediments as well as modern sediments by Mayer (1994), Hedges & Keil (1995), and Keil & Cowie (1999).

The Arbuckle outcrop samples reveal a weaker ($R^2$= 0.58) correlation relative to the core samples. Optical petrography of sample AO-5 (Figure 11b), that plots of the liner regression shows an anomalous amount of OC for the MSA also shows abnormally high fossil abundance possibly containing remnant OM and/or high tasmanite algal cyst abundance that increase OM concentration. This indicates that in some samples, particles of OC recording settling from the water column of detrital OM (at micron-scales) can be preserved along with molecular scale OM associated with mineral surfaces. From this analysis, the vast bulk of the TOC is associated with the mineral surface area and not as discrete and independent particles. Alternatively, some samples

plot with high surface area but with very low TOC (typically <2%) and also plot low of this regression (Figure 9). These samples could be linked to OM oxidation associated with surface weathering of the Arbuckle outcrop (Lo & Cardott 1995). The limited TOC-MSA correlation evident in the East Fitts and Chitwood-Harris samples grouped in the lower (0-4%) TOC range, poorly correlated and homogenised MSA values (40-80 $m^2g^{-1}$) (Figure 9) were subject to level 3-4 bioturbation (Figure 5). Evidence of bioturbation in core and outcrop samples show that intervals in the Chitwood-Harris (4,539-4,545 m and 4,546-4,549 m) were sufficiently aerobic (oxygenated) to support grazing by benthic organisms. Depths of burrows differ, as well as some intervals which show no benthic activity, suggesting that anoxic conditions and resultant hydrogen sulphide ($H_2S$) levels within the sediment fluctuated, and controlled the penetration depth of burrowing organisms (Schinner 1991, Kristensen & Kostka 2005). Biological activity within sediments may have several effects on OC content of sediments such as the mechanical disturbance of a sediment (mixing/homogenisation) allowing irrigation and thus, increasing oxidant within the sediment by influx of oxygenated bottom waters (Aller 1984, Hartnett *et al.* 1998) potentially remineralizing OM (Mackin & Swider 1989, Sandnes *et al.* 2000). Alternatively, The digestive systems of burrowing organisms are capable of altering the mineralogy of sediments including early diagenesis of clay minerals, and the stripping of OM coatings (Worden *et al.* 2006). Variations in bioturbation intensity and the degree of mineralization of OM are apparent in the East Fitts samples which show a correlation between higher index of bioturbation and a low TOC to MSA ratio (Figure 10). The consistent bioturbation throughout the upper zone of the Chitwood-Harris core (4,539-4,545 m) (Figure 5) correlates with a significant reduction of TOC relative to MSA, and homogenization of

MSA compared to the more variable MSA below this interval. In addition, poor to moderate TOC-MSA correlations between 4,545.8 and 4,548.8 m depth of the Chitwood-Harris core also showed minor level 2 bioturbation within massive intervals. A hypothesis offered here is that anoxia acts to keep benthic grazers out of the sediment and thus prevents mineralogical changes and OM removal from some clays during sediment processing in organism digestive systems. It is in these unbioturbated sediments that the retention of a high loading rate of OM on MSA is possible. Consisent with this hypothesis, samples which showed strong ($R^2 = 0.82$ and $R^2 = 0.95$) TOC-MSA correlations did not show indication of bioturbation. It may thus be possible that the primary association between anoxia and OC preservation is not through the common assumption of slowed oxidation rates (Demaison & Moore 1980), but rather through limitation of grazers and the effect of animal digestive systems on sediment mineralogy. While optical and SEM petrography reveal some OC is preserved as tasmanites cysts (organic-rich algal fossils) (Figure 11c, 12a,b). These examples are constrained to localised intervals (Figure 11c) which are sporadic and do not account for the average OM present throughout clay rich intervals which comprise the vast majority of sediment. Discrete (micron-scale) particles from pelagic sources can also not account for the relationship between MSA and TOC which requires that most OM was preserved within the original sediment by mineral surfaces exists as molecular scale compounds. Similar observations in previous studies explain how original bio-productivity driven particulate OM influx controlled by favourable oceanographic nutrient abundance, constitute less than 10% of TOC within continental margin sediments (Hedges & Keil 1995). The removal of particulate OM is attributed to the high rates of biodegradation, and oxidative OM remineralisation within the first10cm of

sediment (Aller 1984, Strohle & Krom 1997) with the remaining molecular OM adsorbed onto mineral surfaces (Hedges & Keil 1995).

Considering the EGME method of measuring MSA uses the principle of the uptake of an organic compound (EGME) into the interlayer sites of expandable clays to measure this surface area, as well as external surfaces of all clay minerals (Kennedy & Wagner 2011), it is reasonable to assume that this can also occur naturally for some types of clay minerals and organic compounds (Cloos *et al.* 1981, Bosetto *et al.* 1997, Alimova *et al.* 2009). The TOC-MSA correlation implies that OM forms an intimate direct relationship with clay mineral surface sites including the abundant surface area associated with interlayers of hydratable clay minerals. This mineral surface adsorption model differs from a particulate spatial association wherein clay mineral aggregates orient in a manner that physically shelters discrete particles of pure OM through encapsulation. Salmon *et al.* (2000) and Ransom *et al.* (1997) suggest the encapsulation of OM by clay aggregates prohibits biological attack and oxidative decomposition leading to enhanced preservation. Using TEM on organic-rich shale ultra-thin sections, Salmon *et al.* (2000) showed that the bulk of OM occurs separately as organic nano-layers (~200 nm thick) primarily associated with clay-rich domains. Similarly, Ransom *et al.* (1997) used TEM on modern sediments to show OM exists as discrete micro-blebs, and bacterial cells. Both studies concluded that OM preservation is primarily constrained to the clay aggregate encapsulation model, but did not find evidence of OM coatings within the clay mineral aggregates, to support the direct mineral surface association model considered here because of technical limitations on sample preparation.

The ultra-thin (80nm) section TEM micrographs (Figure 13, 15) presented here are novel and result from new methods of shale sample preparation using ultramicrotoming

by S. Loehr working in conjunction with the staff at Adelaide Microscopy at the University of Adelaide (S. Loehr pers. comm. 2012). This new approach of imaging using TEM reveals evidence of nanoscale associations between OM and clay minerals in an organic-rich marine shale. The scale of these associations precludes the presence of micron scale particles to explain the presence of OM in a standard example of these samples. EDS spot analysis identifying elemental chemistry at 80 - 100 nm resolution indicated OC was exclusively constrained to clay nanolayers by showing no concentrated zones of OC that were not also associated with Si and Al (Figure 14) identifying a nano-composite phase. Furthermore, closer inspection (120,000 x magnification) (Figure 15) of apparently homogeneous grey zones (<100 nm thick) that would commonly be interpreted as OM particles within clay aggregates similar to those reported by Salmon *et al.* (2000) revealed 10 nm thick illite layers dispersed within these homogenous zones. All areas studied suggested that particles resolved in to clay-organic nanocomposites with closer inspection at higher magnification. This data is important because it directly confirms the physical occurrence of clay-organic nanocomposites in marine organic-rich shales for the first time. Although providing only a 10 by 30 micron scale area of study, this relation can be extrapolated to the rest of the succession by the strong relation between MSA and TOC characterising the bulk properties of the core and outcrop samples of the Woodford Shale. Combined, these two scales of observations strongly support the hypothesised relation between OC preservation through OM adsorption onto clay minerals, as previously proposed for organic-rich black shales by Kennedy *et al.* (2002) and Kennedy & Wagner (2011). Whilst ultramicrotomed diamond cut thin sections enable ~80-100 nm sections of intact sample, highly siliceous samples proved difficult to cut due to their highly resistant and

brittle properties. FIB foils are not subject to this issue due to the unique ion milling processes. The comparison of ultra thin sections prepared using a focused ion beam and microtomed shale ultra-thin sections however, highlights the potential for artefacts that may result from these different types of sample preparation. FIB milling of thin foils showed extensive carbon contamination throughout the sample. EDS on the TEM200 revealed evidence of carbon contamination on quartz grains at the nanoscale. Further investigation revealed that the platinum (Pt) deposited onto the sample prior to ion milling of a thin foil, is an organo-metallic compound (trimethyl-platinum) with a 9:1 C to Pt ratio (Philipp & Rolf 2006, Valizadeh *et al.* 2007). In addition, sample material is redistributed along the thin-section during the milling process, potentially resulting in further carbon contamination (Philipp & Rolf 2006). This raises concerns about C contamination during FIB milling of foils to investigate OM distribution in shales following the Pt strip lift-out method described by Heaney *et al.* (2001), Wirth (2004) and Wirth (2009).

**Quartz Diagenesis and Hydrocarbon Entrapment**

Although potential C contamination of FIB milled thin foils prevented conclusive identification of OM, the broader range of samples which could be prepared in this manner permitted significant TEM observations that may offer an explanation for gas shales serving simultaneously as source rocks and reservoirs. Submicron-scale quartz grain growth and cementation observed in the Chitwood-Harris (Figure 16) was not evident in the East Fitts samples (Figure 13). These observations are supported by XRD results which show authigenic quartz (Table 4) in the thin foils sample (CH-14916.9) and other Chitwood-Harris samples. Authigenic quartz is known to increase in volume through micron to submicron-scale granular overgrowth and cementation within shales

progressively throughout the oil and gas window (Metwally & Chesnokov 2012). This process is primarily attributed to locally precipitated silica-rich fluids discharged by the progressive diagenetic reactions of smectite clay illitization (Peltonen *et al.* 2009, Thyberg *et al.* 2010, Metwally & Chesnokov 2012) which also increases with thermal maturity and is also shown to coincide with the oil and gas window (Pollastro 1993, Williams *et al.* 2005, Abid & Hesse 2007). Silica supply via illitization is a likely cause given the quartz grain-clay juxtapositions evident in the TEM micrograph (Figure 16), and the common presence of illite observed in XRD results (Table 3). In Addition, silica can also be supplied by the dissolution-reprecipitation mechanisms of the diagenetic transition of biogenic silica (opal-A) to microcrystalline silica (opal-CT/-C) during burial (Isaacs 1982, French *et al.* 2012). The support of these studies combined with the TEM micrographs, thermal maturity (%$R_o$ of 1.03), XRD results, and quartz grain-clay juxtapositions, all indicate that the Chitwood-Harris core has undergone micron-scale quartz diagenesis.

Further TEM investigations of quartz grain interactions on the Chitwood-Harris thin foil revealed compartmentalisation of nanoscale zones resulting from quartz overgrowth (Figure 16). It is plausible that the nanoscale compartmentalization operates as a hydrocarbon storage mechanism during thermal maturation in abundant quartz grain zones restricting permeability to zones of reduced quartz grain abundance. This diagenetic quartz related hydrocarbon storage relationship has also been discussed by Metwally & Chesnokov (2012).

In addition, the increased authigenic quartz component increases the shale stiffness tensor, thus increasing hydraulic fracture susceptibility (Thyberg *et al.* 2010, Metwally

& Chesnokov 2012) which directly increases hydrocarbon production rates in shale gas systems (Comer 1991, Curtis 2002, Passey *et al.* 2010, Harris *et al.* 2011). Furthermore, Harris *et al.* (2011) showed that higher quantities of diagenetic silica increased fracture susceptibility when compared to ductile clay-rich zones in the Woodford Shale.

The data here provide compelling evidence for possible controls on OC concentrations in a organic-rich marine shale. In addition, quartz diagenesis observed in TEM petrography may provide an explanation to controls on hydrocarbon storage and fracture susceptibility. The R2 = 0.82 and R2 = 0.95 TOC-MSA correlations supported by visual confirmation of clay-organic nanocomposites, and the quartz diagenesis provide possible answers to multi-scale variables known to control hydrocarbon production. Although the diamond knife cutting difficulties and time necessary to prepare ultramicrotomed thin sections restricted extensive TEM study throughout the sample set, this study highlights the importance of visually confirming known bulk scale correlations particularly at high resolution to resolve the scale of OM-clay interaction.

## CONCLUSIONS

The strong linear correlation between MSA and TOC is consistent with a mineral surface preservative effect on OC extending across the range of samples studied from multiple cores and with TOC values from <0.5% to 18%. This relation implies that OM scales with clay mineral surfaces which occur at the nanometre scale and not as discrete OM particles encapsulated within the shales that are independent of the clay mineral properties. The TEM micrographs of ~80 nm thick ultramicrotomed thin sections provide direct confirmation of clay-organic nanocomposites.

Based on the carbon contamination observed in FIB milled thin foils used in this study, a mindful approach must be taken when interpreting organic matter studies using FIB milled thin foils following the Pt strip lift-out method described by Heaney (2001)Wirth (2004) and Wirth (2009). TEM micrographs of diagenetic quartz grain interactions indicate porosity occlusion which may explain how organic-rich shales can serve contemporaneously as both reservoir and leeching source rock. In addition, the presence of diagenetic quartz enhances fracture susceptibility which is a key factor in hydrocarbon production in shale gas systems.

In summary, the key variable components highlighted in this study; TOC variability, and diagenetic-quartz influencing hydrocarbon storage and fracture susceptibility, all contribute to increased hydrocarbon production, and are all ultimately linked to the proximal presence of clay minerals. By investigating proven gas shales such as the Woodford Shale, the key properties governing successful zones of shale gas production may eventually be identified and utilised to predict potential unconventional hydrocarbon resources in frontier basins.

## ACKNOWLEDGMENTS

I am grateful to my head supervisor Professor Martin Kennedy (University of Adelaide) for making it possible to conduct field work in USA, and for providing overall project scope, advice and thesis support. I am also indebted to my co-supervisor Dr Stefan Löehr (University of Adelaide) for providing project guidance, laboratory assistance, and constructive thesis support. TEM sample preparation and petrographic results would not have been possible without the input of Stefan Löehr, as well as Lyn Waterhouse, Dr Benjamin Wade, Ken Neubauer and Len Green at Adelaide Microscopy. A special thank you to Dr Roger Slatt (Oklahoma University) and Dr Brian Cardott (Oklahoma Geological Survey) for providing research information, core lab access, and warm hospitality during my stay in Oklahoma. I also thank Dr Tony Hall (University of Adelaide) for laboratory management, and GC-MS analysis, and also Dr Rosalind King (University of Adelaide) for course work guidance. Collaborative ideas and experiment assistance by fellow honours student Tom Sturman, and PhD candidate Elizabeth Baruch was greatly appreciated. Sample preparation and geochemical experiments were made possible with the help of laboratory assistants, Robyn Williamson, and lab assistants.

## REFERENCES

ABID I. & HESSE R. 2007. Illitizing fluids as precursors of hydrocarbon migration along transfer and boundary faults of the Jeanne d'Arc Basin offshore Newfoundland, Canada. *Marine and Petroleum Geology* **24**, 237-245.

ABOUSLEIMAN Y., TRAN M., HOANG S., BOBKO C., ORTEGA A. & ULM F. J. 2007. Geomechanics field and laboratory characterization of woodford shale: The next gas play, pp. 2127-2140.

ALEXANDER R., KAGI R. I. & LARCHER A. V. 1982. Clay catalysis of aromatic hydrogen-exchange reactions. *Geochimica et Cosmochimica Acta* **46**, 219-222.

ALEXANDER R., KAGI R. I. & LARCHER A. V. 1984. Clay catalysis of alkyl hydrogen exchange reactions—reaction mechanisms. *Organic Geochemistry* **6**, 755-760.

ALIMOVA A., KATZ A., STEINER N., RUDOLPH E., WEI H., STEINER J. C. & GOTTLIEB P. 2009. Bacteria-clay interaction: structural changes in smectite induced during biofilm formation. *Clays and Clay Minerals* **57**, 205-212.

ALLER R. C. 1984. The importance of relict burrow structures and burrow irrigation in controlling sedimentary solute distributions. *Geochimica et Cosmochimica Acta* **48**, 1929-1934.

ALTANER S. P. & YLAGAN R. F. 1997. Comparison of structural models of mixed-layer illite/smectite and reaction mechanisms of smectite illitization. *Clays and Clay Minerals* **45**, 517-533.

ARTHUR M. A. & SAGEMAN B. B. 1994. Marine black shales: a review of depositional mechanisms and significance of ancient deposits. *Earth Planet* **22**, 499-551.

BAUMGART A., JENNERJAHN T., MOHTADI M. & HEBBELN D. 2010. Distribution and burial of organic carbon in sediments from the Indian Ocean upwelling region off Java and Sumatra, Indonesia. *Deep Sea Research Part I: Oceanographic Research Papers* **57**, 458-467.

BERMAN A. 2009. *Lessons from the Barnett Shale suggest caution in other shale plays*. *World Oil Magazine*.

BERNER R. A. 1989. Biogeochemical cycles of carbon and sulfur and their effect on atmospheric oxygen over phanerozoic time. *Palaeogeography, Palaeoclimatology, Palaeoecology* **75**, 97-122.

BLACKMAN A., BOTTLE S., SCHMID S., MOCERINO M. & WILLE U. 2008. *Chemistry*. John Wiley & Sons Australia, Limited, Australia.

BLAKEY R. C. 2008. Paleogeography and geologic evolution of North America. *[Web page]; North American Paleogeographic Maps <http://jan.ucc.nau.edu/~rcb7/nam.html> Date accessed 25th May 2012*.

BOSETTO M., ARFAIOLI P., PANTANI O. L. & RISTORI G. G. 1997. Study of the humic-like compounds formed from L-tyrosine on homoionic clays. *Clay Minerals*, 341-349.

BROADHEAD R. F. 2010. The Woodford Shale in southeastern New Mexico: Distribution and source rock characteristics. *New Mexico Geology* **32**, 79-90.

BURDIGE D. J. 2007. Preservation of organic matter in marine sediments: Controls, mechanisms, and an imbalance in sediment organic carbon budgets? *Chemical Reviews* **107**, 467-485 <http://www.scopus.com/inward/record.url?eid=2-s2.0-33847721392&partnerID=40&md5=031083f06667d0212711212b1a7b94fe>.

CANFIELD D. E. 1994. Factors influencing organic carbon preservation in marine sediments. *Chemical Geology* **114**, 315-329 DOI: 10.1016/0009-2541(94)90061-2 <http://www.sciencedirect.com/science/article/pii/0009254194900612>.

CARDOTT B. J. & CHAPLIN J. R. 1993. Guidebook for Selected Stops in the Western Arbuckle Mountains, Southern Oklahoma. *Oklahoma Geological Survey - Special Publication* **93**, 1-54.

CLOOS P., BADOT C. & HERBILLON A. 1981. Interlayer formation of humin in smectites. *Nature* **289**, 391-393.

COMER J. B. 1991. Stratigraphic Analysis of the Upper Devonian Woodford Formation, Permian Basin, West Texas and Southeastern New Mexico. *Bureau of Economic Geology* **201**, 1-66.

COMER J. B. 2008. Woodford Shale in Southern Midcontinent, USA - Transgressive System Tract Marine Source Rocks on an Arid Passive Continental Margin with Persistent Oceanic Upwelling. *Poster, AAPG Annual Meeting.*

COOKE D. 2011. The production rate variability problem with shale reservoirs: what we know and what we don't know. *CSIRO Publication* **2011**, 22-27.

COPPOLA L., GUSTAFSSON Ö., ANDERSSON P., EGLINTON T. I., UCHIDA M. & DICKENS A. F. 2007. The importance of ultrafine particles as a control on the distribution of organic carbon in Washington Margin and Cascadia Basin sediments. *Chemical Geology* **243**, 142-156.

CURRY K. J., BENNETT R. H., MAYER L. M., CURRY A., ABRIL M., BIESIOT P. M. & HULBERT M. H. 2007. Direct visualization of clay microfabric signatures driving organic matter preservation in fine-grained sediment. *Geochimica et Cosmochimica Acta* **71**, 1709-1720.

CURTIS J. B. 2002. Fractured shale-gas systems. *Aapg Bulletin* **86**, 1921-1938.

DEMAISON G. J. & MOORE G. T. 1980. Anoxic environments and oil source bed genesis. *Organic Geochemistry* **2**, 9-31.

DROSER M. L. & BOTTJER D. J. 1993. Trends and Patterns of Phanerozoic Ichnofabrics. *Annual Review of Earth and Planetary Sciences* **21**, 205-225.

DURHAM L. D. 2010. Shales – Similar, Yet So Different <http://www.aapg.org/explorer/2010/09sep/shalegas0910.cfm>. Date accessed 20th September 2012.

EIA 2012. U.S. Crude Oil, Natural Gas, and NG Liquids Proved Reserves <http://www.eia.gov/naturalgas/crudeoilreserves/>. (retrieved October 6th 2012).

EIA U. S. 2011. Review of Emerging Resources: U.S. Shale Gas and Shale Oil Plays. *U.S. Department of Energy, Washington, DC*, 1-105.

ESLINGER E. V., MAYER L. M., THOMAS L. D., HOWER J. & SAVIN S. M. 1973. An X-ray Technique for Distinguishing Between Detrital and Secondary Quartz in the Fine-grained Fraction of Sedimentary Rocks. *Journal of Sedimentary Petrology* **43**, 540-543.

FRENCH M. W., WORDEN R. H., MARIANI E., LARESE R. E., MUELLER R. R. & KLIEWER C. E. 2012. Microcrystalline Quartz Generation and the Preservation of Porosity In Sandstones: Evidence from the Upper Cretaceous of the Subhercynian Basin, Germany. *Journal of Sedimentary Research* **82**, 422-434.

HARRIS N. B., MISKIMINS J. L. & MNICH C. A. 2011. Mechanical anisotropy in the Woodford Shale, Permian Basin: Origin, magnitude, and scale. *Leading Edge* **30**.

HART B., SAYERS C. M. & JACKSON A. 2011. An Introduction to this Special Section: Shales. *Society of Exploration Geophysicists - Leading Edge* **30**, 272-273.

HARTNETT H. E., KEIL R. G., HEDGES J. I. & DEVOL A. H. 1998. Influence of oxygen exposure time on organic carbon preservation in continental margin sediments. *Nature* **391**, 572-575.

HEANEY P. J., VICENZI E. P., GIANNUZZI L. A. & LIVI K. J. T. 2001. Focused ion beam milling: A method of site-specific sample extraction for microanalysis of Earth and planetary materials. *American Mineralogist* **86**, 1094-1099.

HEDGES J. I. & KEIL R. G. 1995. Sedimentary organic matter preservation: an assessment and speculative synthesis. *Marine Chemistry* **49**, 81-115.

HIGLEY D. K. 2011. *Undiscovered Petroleum Resources for the Woodford Shale and Thirteen Finger Limestone–Atoka Shale Assessment Units, Anadarko Basin*. U.S. Geological Survey Open File Report 2011–1242, U.S.G.S.

HUNT J. M. 1996. *Petroleum geochemistry and geology*. W. H. Freeman and Company, New York.

ISAACS C. M. 1982. Influence of rock composition on kinetics of silica phase changes in the Monterey Formation, Santa Barbara area, California. *Geology* **10**, 304-308.

JAHN F., COOK M. & GRAHAM M. 2008. *Hydrocarbon Exploration and Production* (2 edition). (Developments in Petroleum Geoscience). Elsevier.

JENKINS C. D. & BOYER C. M. 2008. Coalbed- and Shale-Gas Reservoirs. *Society of Petroleum Engineers - Journal of Petroleum Technology* **Distinguished Author Series**, 92-99.

JOHNS W. D. 1979. Clay mineral catalysis and petroleum generation. *Annual review of earth and planetary sciences, Vol. 7*, 183-198.

KEIL R. G. & COWIE G. L. 1999. Organic matter preservation through the oxygen-deficient zone of the NE Arabian Sea as discerned by organic carbon:mineral surface area ratios. *Marine Geology* **161**, 13-22.

KEIL R. G., MONTLUCON D. B., PRAHL F. G. & HEDGES J. I. 1994. Sorptive Preservation of Labile Organic Matter in Marine Sediments. *Nature* **370**, 549-552.

KENNEDY M., DROSER M. M., L. M., PEVEAR D. & MROFKA D. 2006. Late precambrian oxygenation; inception of the clay mineral factory. *Science* **311**, 1446-1449.

KENNEDY M. J., PEVEAR D. R. & HILL R. J. 2002. Mineral Surface Control of Organic Carbon in Black Shale. *Science* **295**, 657.

KENNEDY M. J. & WAGNER T. 2011. Clay mineral continental amplifier for marine carbon sequestration in a greenhouse ocean. *PNAS* **108**, 9776-9781.

KRISTENSEN E. & KOSTKA J. E. 2005. Macrofaunal Burrows and Irrigation in Marine Sediment: Microbiological and Biogeochemical Interactions. *The Ecogeomorphology of Tidal Marshes Coastal and Estuarine Studies* **59**, 1-36.

KULKARNI P. 2011. Developing the Woodford - An unconventional play with conventional exploration and production constraints. *Shale Energy*, 93-98.

KUYKENDALL R. D. F. A. M. D. 2001. Misener Sandstone of Oklahoma. *Oklahoma Geological Survey Special Publication* **93**, 117-134.

LALLIER-VERGÈS E., BERTRAND P., HUC A. Y., BÜCKEL D. & TREMBLAY P. 1993. Control of the preservation of organic matter by productivity and sulphate reduction in Kimmeridgian shales from Dorset (UK). *Marine and Petroleum Geology* **10**, 600-605.

LANSON B., SAKHAROV B. A., CLARET F. & DRITS V. A. 2009. Diagenetic smectite-to-illite transition in clay-rich sediments: A reappraisal of x-ray diffraction results using the multi-specimen method. *American Journal of Science* **309**, 476-516.

LEWAN M. D. 1983. Effects of thermal maturation on stable organic carbon isotopes as determined by hydrous pyrolysis of Woodford Shale. *Geochimica et Cosmochimica Acta* **47**, 1471-1479.

LO H. B. & CARDOTT B. J. 1995. Detection of natural weathering of Upper McAlester coal and Woodford Shale, Oklahoma, U.S.A. *Organic Geochemistry* **22**, 73-83.

LOEHR S. C. 2012. Fraser S. A., University of Adelaide.

MACKIN J. E. & SWIDER K. T. 1989. Organic matter decomposition pathways and oxygen consumption in coastal marine sediments. *Journal of Marine Research* **47**, 681-716.

MAYER L. M. 1993. Relationships between mineral surfaces and organic carbon concentrations in soils and sediments. *Chemical Geology* **114**, 347-363.

MAYER L. M. 1994. Surface area control of organic carbon accumulation in continental shelf sediments. *Geochimica et Cosmochimica Acta* **58**, 1271-1284.

METWALLY Y. M. & CHESNOKOV E. M. 2012. Clay mineral transformation as a major source for authigenic quartz in thermo-mature gas shale. *Applied Clay Science* **55**, 138-150.

MOORE M. & REYNOLDS R. C. J. 1989. *X-Ray Diffraction and the identification and Analysis of Clay Minerals*. Oxford University Press, Oxford New York.

NETL 2011. Shale Gas: Applying Technology to Solve America's Energy Challenges.

PASSEY Q. R., BOHACS K. M., ESCH W. L., KLIMENTIDIS R. & SINHA S. 2010. From Oil-Prone Source Rock to Gas-Producing Shale Reservoir - Geologic and Petrophysical Characterization of Unconventional Shale Gas Reservoirs. *Society of Petroleum Engineers - Conference Paper*, 1-29.

PELTONEN C., MARCUSSEN Ø., BJØRLYKKE K. & JAHREN J. 2009. Clay mineral diagenesis and quartz cementation in mudstones: The effects of smectite to illite reaction on rock properties. *Marine and Petroleum Geology* **26**, 887-898.

PETERS K. E., WALTERS C. C. & MOLDOWAN J. M. 2005. *The Biomarker Guide Volume 2 Biomarkers and Isotopes in Petroleum Systems and Earth History* (Vol. 2). Cambridge University Press.

PHILIPP M. N. & ROLF B. 2006. Milling micro-structures using focused ion beams and its application to photonic components. *Measurement Science and Technology* **17**, 943.

POLLASTRO R. M. 1993. Considerations and Applications of the Illite/Smectite Geothermometer in Hydrocarbon-bearing Rocks of Miocene to Mississippian Age. *Clays and Clay Minerals* **41**, 119-133.

POPPE L. J., PASKEVICH V. F., HATHAWAY J. C. & BLACKWOOD D. S. 2001. A Laboratory Manual for X-Ray Powder Diffraction. *Open-File Report 01-041*.

RANSOM B., BENNETT R. H., BAERWALD R. & SHEA K. 1997. TEM study of in situ organic matter on continental margins: occurrence and the "monolayer" hypothesis. *Marine Geology* **138**, 1-9.

RANSOM B., KIM D., KASTNER M. & WAINWRIGHT S. 1998. Organic matter preservation on continental slopes: importance of mineralogy and surface area. *Geochimica et Cosmochimica Acta* **62**, 1329-1345.

ROHLING E. J. 1991. Shoaling of the Eastern Mediterranean Pycnocline due to reduction of excess evaporation: Implications for sapropel formation. *Palaeoceanography* **6**, 747.

ROMERO A. M. & PHILP R. P. 2012. Organic geochemistry of the Woodford Shale, southeastern Oklahoma: How variable can shales be? *Aapg Bulletin* **96**, 493-517.

SAGEMAN B. B., MURPHY A. E., WERNE J. P., VER STRAETEN C. A., HOLLANDER D. J. & LYONS T. W. 2003. A tale of shales: the relative roles of production, decomposition, and dilution in the accumulation of organic-rich strata, Middle–Upper Devonian, Appalachian basin. *Chemical Geology* **195**, 229-273.

SALMON V., DERENNE S., LALLIER-VERGÈS E., LARGEAU C. & BEAUDOIN B. 2000. Protection of organic matter by mineral matrix in a Cenomanian black shale. *Organic Geochemistry* **31**, 463-474.

SANDNES J., FORBES T., HANSEN R., SANDNES B. & RYGG B. 2000. Bioturbation and irrigation in natural sediments, described by animal-community parameters. *Marine Ecology Progress Series* **197**, 169-179.

SCHINNER G. O. 1991. Burrowing Behavior, Substratum Preference, and Distribution of Schizaster canaliferus (Echinoidea: Spatangoida) in the Northern Adriatic Sea. *Marine Ecology* **14**, 129-145.

SHERROD L. A., DUNN G., PETERSON G. A. & KOLBERG R. L. 2002. Inorganic Carbon Analysis By Modified Pressure-calcimeter Method. *Soil Sci. Soc. Am. J.* **66**, 299-305.

SLATT R., ROMINA PORTAS, NICHOLE BUCKNER, YOUNANE ABOUSLEIMAN, NEAL O'BRIEN, MINH TRAN, RAFAEL SIERRA, PAUL PHILP, ANDREA MICELI-ROMERO, ROBERT DAVIS & WAWRZYNIEC T. 2011. Outcrop/Behind Outcrop (Quarry), Multiscale Characterization of the Woodford Gas Shale, Oklahoma. *AAPG Conference and Exhibition Presentation*, 1-22.

SMITH M. G. & BUSTIN R. M. 1998. Production and preservation of organic matter during deposition of the Bakken Formation (Late Devonian and Early Mississippian), Williston Basin. *Palaeogeography, Palaeoclimatology, Palaeoecology* **142**, 185-200.

STANLEY D. J. 1978. Ionian Sea sapropel distribution and late Quaternary palaeoceanography in the eastern Mediterranean. *Nature* **274**, 149-152.

STROHLE K. & KROM M. D. 1997. Evidence for the evolution of an oxygen minimum layer at the beginning of S-1 sapropel deposition in the eastern Mediterranean. *Marine Geology* **140**, 231-236.

THYBERG B., JAHREN J., WINJE T., BJØRLYKKE K., FALEIDE J. I. & MARCUSSEN Ø. 2010. Quartz cementation in Late Cretaceous mudstones, northern North Sea: Changes in rock properties due to dissolution of smectite and precipitation of micro-quartz crystals. *Marine and Petroleum Geology* **27**, 1752-1764.

TILLER K. G., SMITH, L.H. 1990. Limitations of EGME Retention to Estimate the Surface Area of Soils. *Soil Chemistry and Mineralogy*, 1-26.

TISSOT B. P., PELET R. & UNGERER P. H. 1987. Thermal history of sedimentary basins, maturation indices, and kinetics of oil and gas generation. *AAPG Bulletin* **71**, 1445–1466.

TYSON R. V. 2001. Sedimentation rate, dilution, preservation and total organic carbon: some results of a modelling study. *Organic Geochemistry* **32**, 333-339.

VALIZADEH S., ABID M., HERNÁNDEZ-RAMÍREZ F., RODRÍGUEZ A. R., HJORT K. & SCHWEITZ J. Å. 2007. Template synthesis and forming electrical contacts to single Au nanowires by focused ion beam techniques. *Nanotechnology* **18**, 459001.

WILLIAMS L. B., CANFIELD B., VOGLESONGER K. M. & HOLLOWAY J. R. 2005. Organic molecules formed in a "primordial womb". *Geology* **33**, 913-916.

WILLIAMS L. B., HERVIG R. L., HOLLOWAY J. R. & HUTCHEON I. 2001. Boron isotope geochemistry during diagenesis. Part I. Experimental determination of fractionation during illitization of smectite. *Geochimica et Cosmochimica Acta* **65**, 1769-1782.

WIRTH R. 2004. Focused Ion Beam (FIB): A novel technology for advanced application of micro- and nanoanalysis in geosciences and applied mineralogy. *European Journal of Mineralogy* **16**, 863-876.

WIRTH R. 2009. Focused Ion Beam (FIB) combined with SEM and TEM: Advanced analytical tools for studies of chemical composition, microstructure and crystal structure in geomaterials on a nanometre scale. *Chemical Geology* **261**, 217-229.

WORDEN R. H., NEEDHAM S. J. & CUADROS J. 2006. The worm gut; a natural clay mineral factory and a possible cause of diagenetic grain coats in sandstones. *Journal of Geochemical Exploration* **89**, 428-431.

# APPENDIX A: METHODS

## Ethylene Glycol Monoethyl Ether - Mineral Surface Area

EGME derived mineral surface area (MSA) adapted from Tiller & Smith (1990) is reported as 'free surface' dehydrated silicate MSA on a OC and carbonate free basis to avoid the effects of carbonate dilution which could result in an auto correlation between TOC and MSA. Carbonate does not have a significant surface area (<15 $m^2g^{-1}$) and can result from post burial processes.

Method:

From each sample, a 10g subsample was removed by chipping or diamond saw.
Each subsample was crushed using a mechanical mill, which was carefully cleaned with water, compressed air, and ethanol between each sample to avoid cross contamination.
Milled samples were ground into a uniform grain size powder through use of mortar and pestle, and a fine (0.0097 inch) sieve.
Ground samples were stored individually in sealed and labeled vials.

EGME MSA measurement requires four main stages which includes the following:
Calcium exchange of ground samples
Record vial and oven-dry sample mass prior to exposure to EGME
Equilibration with EGME in vacuum chamber
Vial weighing to determine mass EGME retained by sample

The calcium exchange procedure standardizes the exchangeable cations in all samples and standardization is required because EGME retention is dependent on the exchangeable cations in samples.

Calcium exchange procedure:

Weigh 1.1g of ground sample into corresponding centrifuge tube (sample).
Add 15ml of $CaCl_2$ solution to each sample and shake until sufficiently mixed.
Put centrifuge tubes into end-over-end shaker for 10 minutes.

Let samples rest for 1 hour.
Add de-ionized water to 50 ml mark to each centrifuge tube.
Centrifuge samples at 3000rpm for 15 minutes (mins). This process separates the shale sample forming a compact solid at the bottom of the centrifuge tube.
Carefully pour off supernatant solution into appropriate waste vessel, avoiding loss of sample solid.
Add 45ml (45ml to indicate procedure phase) of DI water and shake centrifuge tube until sample is completely suspended and centrifuge. Pour out supernatant
Repeat step 7.
Leave the sample solid in the tube and store in a drying oven at 40˚C until dry.
Individually remove sample from each tube and regrind, then place back in the oven to prevent moisture absorbing into the sample.

The samples are now prepared for the EGME vacuum retention experiment.

Labelling and weighing sample vials for EGME vacuum retention:
Wearing gloves, label glass scintillation vials and caps with a corresponding sample numbers/names with a diamond pen and engraving scribe respectively.
Weigh each vial, and its assigned lid separately on an analytical balance to a five decimal places
Document each weight for each vial in a table (e.g. shown below)

**Sample series:** **Date:**

| Sample No. | Empty vial weight (g) | Cap weight (g) | Total weight (g) | Sample weight (g) | Sample weight with EGME (g) |
|---|---|---|---|---|---|
| | | | | | |
| | | | | | |
| | | | | | |

Wearing gloves, place 1 gram (g) of sample into their respective vials.
Place vials with samples into drying oven overnight.
Remove vials from oven and cap quickly, leave to cool in a desiccator.
Weigh capped vials containing sample once cooled.
Within a fume cupboard, place 1ml of EGME into each vial.
Leaving lids off, place vials into a vacuum chamber with lids on a separate tray in layout mimicking the layout of vials to easily identify corresponding lids when applying lids at the end of the experiment. Lids need not be placed in vacuum chamber.
Add 40mls of EGME to a beaker, and place at the top of the vacuum chamber.
Place 200g of granular $CaCl_2$ at the base of the vacuum chamber.
Close vacuum chamber and evacuate chamber for 10 minutes.
Leave vials for a period of 2 weeks, replacing the EGME beaker and granular $CaCl_2$ solids as needed. CaCl2 may need replacing every 2 days if it forms a surface crust and no longer absorbs surplus EGME.

Vial weighing for EGME retention mass gain:

After 2 weeks, slowly re-pressurize chamber and remove vials, replacing lids onto each corresponding vial as quickly as possible so as to minimize moisture sorption from atmosphere.
Weigh each vial recording the mass gain change in the table previously drafted. Replace vials back in chamber with lid removed and evacuate chamber.
Repeat removal and weighing process every 2 days until mass gain for samples has stabilized.
Record stabilized weight. Surface area is calculated utilizing the mass gain of EGME retention into sample.

## GC-MS Thermal Maturity

For each analysis, powdered sample (approx 10 mg) was transferred to a pre-cleaned MSSV glass reactor tube (high purity silica, sealed at one end, with an internal volume of 100 µl and bent at approximately 120º in the middle). The tube dead volume was filled with pre-cleaned, 80–120 mesh, glass beads and the tube sealed with a high-temperature propane torch. Samples to undergo investigation by pyrolysis were thermally cleaned at 300ºC for 1 hour prior to insertion into the MSSV tube to remove the extractable fraction, once sealed in the reactor vessel they were then transferred to a high precision oven and heated for 24 hr at 325ºC. Analyses were undertaken utilising a Quantum MSSV injector fitted to a Hewlett Packard 6890/5973 gas chromatograph-mass spectrometer (GC-MS) system. An HP5-MS capillary column of 25 m length, 0.25 mm ID and 0.25 µdf coating was used for the separations with helium carrier gas at a constant pressure of 60 KPa. Reactor tubes were inserted into the injector heated at 300ºC and taken through a cleaning cycle of the GC by heating from 45 to 300ºC at 15ºC/min before holding at 300ºC for 15 min to remove any contaminants from the exterior of the tubes. This cleaning cycle also served as the thermal desorption stage for non-pyrolysed samples including additional dwell time to extend the overall period to 1 hr. The tubes were then cracked open within the injector, operating in splitless mode for 2 min, with the released analytes cryofocused in the front of the capillary column using a liquid nitrogen bath. GC-MS analysis was conducted, in full scan mode, employing a temperature program of 45 to 300ºC at 8ºC/min, then held isothermal for 17 min. Full scan data were acquired over a range of 45 to 450 amu at approximately 3 scans per sec.

# APPENDIX B: RESULTS

## Geochemical Data Summary

East Fitts Results

| Depth conversion (m) | Sample ID | Carbonate % | TOC% C Corr. | Silicate MSA (m2/g) |
|---|---|---|---|---|
| 1032.7 | 3388 | 10.51 | 6.92 | 111.12 |
| 1033.2 | 3389.9 | 10.08 | 8.57 | 128.26 |
| 1035.1 | 3395.9 | 5.21 | 9.31 | 133.01 |
| 1035.8 | 3398.2 | 6.89 | 7.83 | 129.32 |
| 1036.0 | 3398.9 | 8.44 | 8.02 | 167.23 |
| 1037.2 | 3403 | 12.14 | 4.36 | 107.57 |
| 1037.8 | 3405 | 4.37 | 8.39 | 126.02 |
| 1038.1 | 3406 | 4.59 | 11.86 | 161.24 |
| 1039.0 | 3408.7 | 17.40 | 10.42 | 151.26 |
| 1039.3 | 3409.9 | 4.66 | 14.60 | 195.62 |
| 1039.9 | 3411.9 | 6.26 | 7.77 | 129.02 |
| 1040.0 | 3412 | 6.38 | 11.98 | 148.00 |
| 1040.7 | 3414.4 | 5.36 | 10.14 | 143.36 |
| 1040.9 | 3415 | 5.49 | 7.99 | 133.77 |
| 1041.4 | 3416.8 | 5.72 | 8.98 | 139.55 |
| 1041.5 | 3417.1 | 5.13 | 16.51 | 235.11 |
| 1041.6 | 3417.3 | 4.66 | 13.75 | 216.30 |
| 1041.8 | 3417.9 | 5.26 | 1.08 | 102.87 |
| 1042.4 | 3420.1 | 4.75 | 2.47 | 126.42 |
| 1043.1 | 3422.4 | 5.65 | 0.83 | 102.75 |

Chitwood-Harris Results

| Depth conversion (m) | Sample ID | Carbonate % | TOC C Corr. | Silicate MSA (m2/g) |
|---|---|---|---|---|
| 4539.33 | 14892.8 | 3.73 | 5.09 | 68.63 |
| 4539.69 | 14894.0 | 4.16 | 4.53 | 63.79 |
| 4540.94 | 14898.1 | 7.23 | 0.84 | 18.31 |
| 4541.64 | 14900.4 | 7.34 | 0.54 | 8.44 |
| 4541.70 | 14900.6 | 7.00 | 5.47 | 65.88 |
| 4541.95 | 14901.4 | 7.87 | 4.78 | 51.71 |
| 4542.53 | 14903.3 | 8.72 | 5.86 | 69.75 |
| 4542.86 | 14904.4 | 6.06 | 3.87 | 42.45 |
| 4543.50 | 14906.5 | 8.13 | 1.41 | 25.92 |
| 4544.02 | 14908.2 | 10.41 | 5.66 | 61.85 |
| 4544.81 | 14910.8 | 15.00 | 1.96 | 35.19 |
| 4544.93 | 14911.2 | 5.22 | 1.08 | 15.48 |
| 4545.15 | 14911.9 | 3.33 | 4.28 | 60.25 |
| 4545.42 | 14912.8 | 3.26 | 1.64 | 35.02 |
| 4545.45 | 14912.9 | 4.80 | 6.49 | 81.71 |
| 4545.63 | 14913.5 | 5.16 | 5.32 | 58.92 |
| 4545.82 | 14914.1 | 3.35 | 1.78 | 24.78 |
| 4546.43 | 14916.1 | 3.27 | 2.35 | 30.33 |
| 4546.67 | 14916.9 | 3.50 | 10.23 | 117.08 |
| 4546.85 | 14917.5 | 3.42 | 2.84 | 52.20 |
| 4547.10 | 14918.3 | 2.73 | 1.88 | 22.70 |
| 4547.49 | 14919.6 | 15.72 | 0.38 | 46.06 |
| 4547.71 | 14920.3 | 3.35 | 0.62 | 54.93 |
| 4548.38 | 14922.5 | 5.24 | 0.61 | 58.40 |
| 4548.80 | 14923.9 | 3.27 | 0.85 | 37.77 |
| 4549.08 | 14924.8 | 3.35 | 0.53 | 58.04 |
| 4549.14 | 14925.0 | 3.42 | 0.91 | 56.84 |
| 4549.44 | 14926.0 | 3.79 | 0.61 | 56.29 |
| 4549.69 | 14926.8 | 3.11 | 0.49 | 48.10 |
| 4549.93 | 14927.6 | 3.41 | 0.69 | 48.03 |
| 4549.99 | 14927.8 | 3.42 | 0.55 | 47.47 |
| 4550.33 | 14928.9 | 6.16 | 1.43 | 40.23 |
| 4550.63 | 14929.9 | 3.19 | 0.00 | 34.54 |
| 4550.97 | 14931.0 | 3.35 | 5.34 | 84.64 |
| 4551.27 | 14932.0 | 3.49 | 4.92 | 79.49 |
| 4551.58 | 14933.0 | 3.27 | 5.43 | 80.27 |
| 4551.76 | 14933.6 | 3.33 | 5.14 | 83.11 |
| 4552.16 | 14934.9 | 3.19 | 5.50 | 80.94 |
| 4552.19 | 14935.0 | 3.12 | 4.13 | 89.70 |
| 4552.61 | 14936.4 | 3.35 | 2.83 | 66.17 |
| 4553.44 | 14939.1 | 3.20 | 4.06 | 83.41 |

Arbuckle Outcrop Results

| Sample | Carbonate % | TOC% C Corr. | Silicate MSA (m2/g) |
|---|---|---|---|
| 3-23-00/1 | 1.60 | 0.00 | 50.07 |
| 3-23-00/2 | 0.86 | 17.84 | 288.54 |
| 3-23-00/3 | 0.93 | 0.25 | 128.31 |
| 3-23-00/6 | 1.01 | 11.22 | 126.62 |
| 3-23-00/8R | 0.93 | 9.90 | 143.22 |
| 3-23-00/9R | 1.00 | 4.91 | 110.61 |
| 3-23-00/10A | 0.70 | 4.92 | 91.65 |
| 3-23-00/10B | 1.37 | 9.85 | 154.52 |
| 3-23-00/11R | 1.16 | 3.89 | 39.29 |
| 3-23-00/12 | 0.93 | 0.19 | 83.08 |
| 3-23-00/13 | 1.09 | 0.27 | 75.66 |
| 3-23-00/14 | 17.72 | 7.83 | 133.92 |
| 3-23-00/15 | 1.32 | 13.31 | 163.82 |
| 3-23-00/17 | 0.79 | 11.44 | 177.55 |
| 3-23-00/19 | 1.17 | 11.62 | 154.06 |
| 3-23-00/20 | 1.45 | 12.20 | 144.23 |
| 3-23-00/21 | 1.00 | 14.51 | 189.00 |
| 3-23-00/22 | 1.25 | 17.03 | 190.22 |
| 3-23-00/23 | 1.08 | 11.99 | 144.43 |
| 3-23-00/24 | 0.86 | 15.75 | 138.32 |
| 3-23-00/25 | 1.39 | 12.57 | 82.42 |
| 3-23-00/28 | 5.94 | 5.98 | 129.65 |
| 3-23-00/29 | 8.01 | 1.81 | 95.95 |
| 3-23-00/31 | 1.01 | 0.65 | 96.59 |

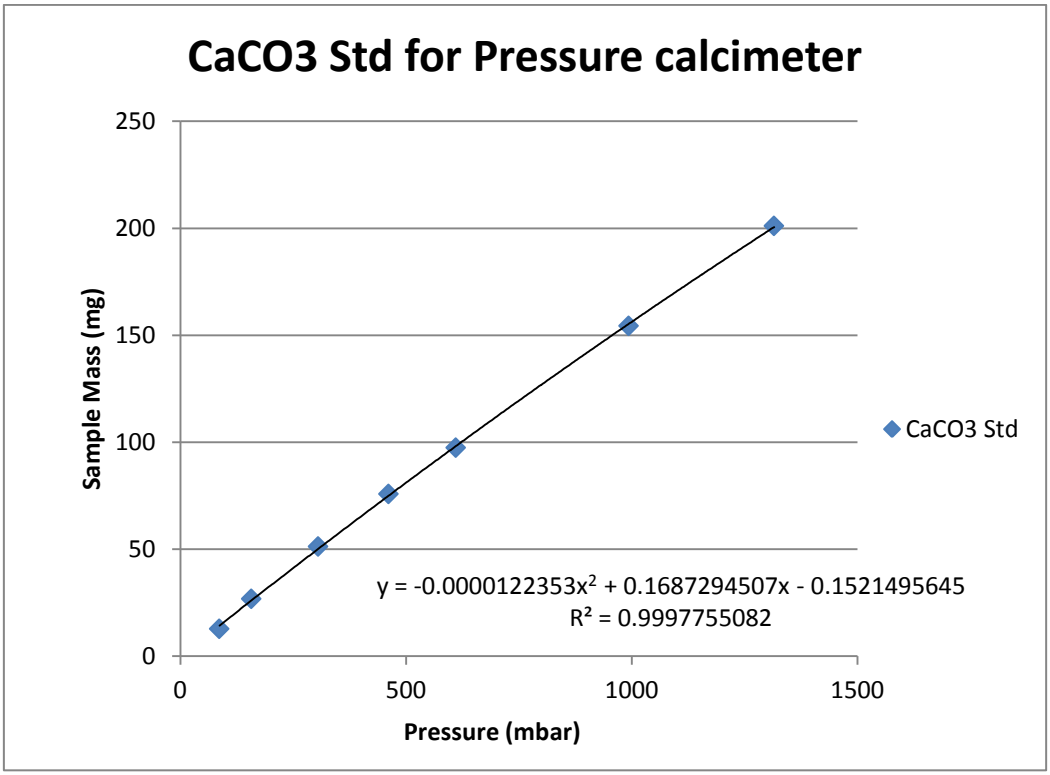


**Figure B1 CaCO3 standards tested and plot for pressure calcimeter calibration to determine calcium carbonate content following methods by Tiller & Smith (1990).**

## GC-MS MPI Thermal Maturity

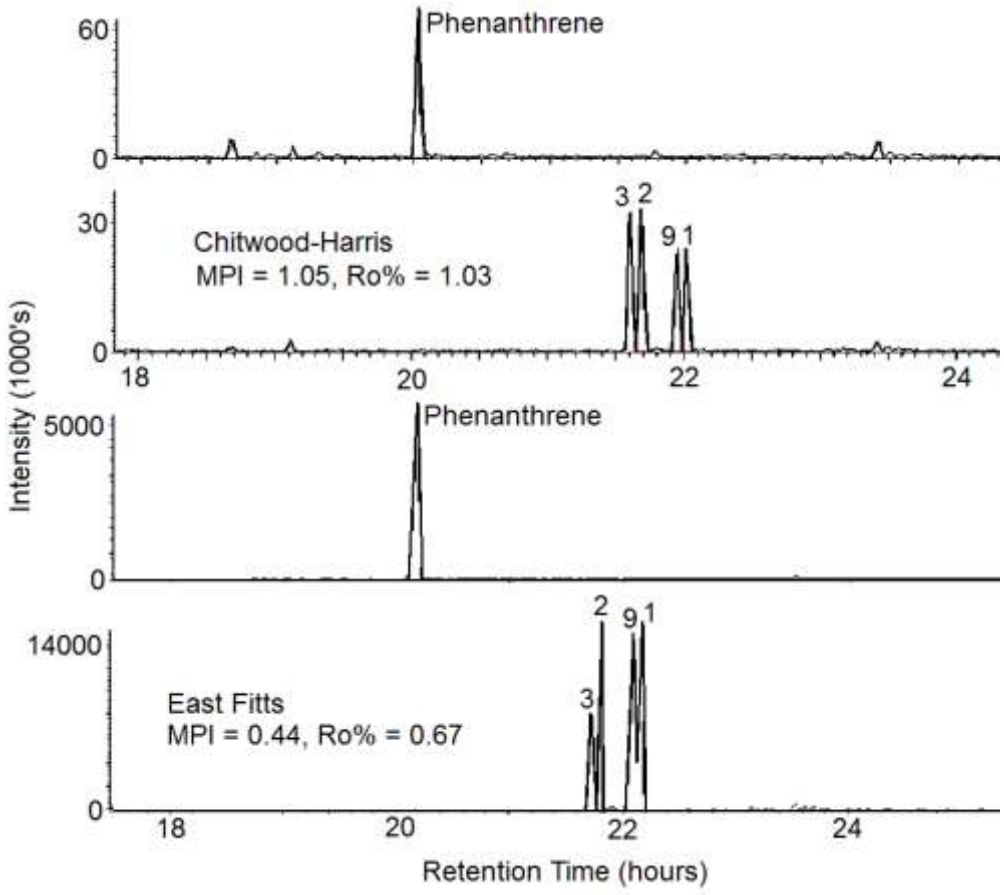


**Figure B2: Gas chromatograms of Chitwood-Harris and East Fitts samples used to calculate thermal maturity for petroleum generation based on peak values of phenanthrene and methylphenanthrene peaks following methods by Peters *et al.* (2005). Chitwood-Harris shows a calculated vitrinite reflectance (Ro%) of 1.03 indicating the core is within the liquid petroleum generation window which ranges between 0.5-0.6%$R_o$ to 1.3-1.35%$R_o$. East Fitts shows a calculated Ro% of 0.67 indicating the core began entering the oil window.**